THE EROSION PROCESS OF COHESIVE SOIL DUE TO A SUBMERGED INCLINED WATER JET

To obtain the degree of Master of Science
at Delft University of Technology,
to be defended in public on Thursday, February 29, 2024 at 13:00.

by

Andrew L. SNYDER

Masters Student in Dredging Engineering,
Delft University of Technology, Delft, the Netherlands,
born in Cincinnati, Ohio, United States of America.

Student Number: 5237521

This thesis has been approved by the

supervisor: Dr. ir. S. Alhaddad
co-supervisor: Prof. dr. ir. C. van Rhee
co-supervisor: Dr. ir. G.H. Geert Keetels

Composition of the Thesis committee:

Dr. ir. G.H. Geert Keetels,	Chairman
Dr. ir. S. Alhaddad,	Assistant Professor
ir. Sterre Bult,	PhD Candidate, Technische Universiteit Delft

Keywords: Cohesive soil, Moving Jet, Inclined Jet, Erosion, Polymetallic Nodules, Deep-sea Mining...

An electronic version of this Thesis is available at
http://repository.tudelft.nl/.

Acknowledgements

I would like to express my gratitude to my main advisor, Professor Said Alhadad, whose guidance, expertise, encouragement, and support have been invaluable throughout the entire research process. His dedication to my academic growth and his insightful feedback have significantly contributed to the quality of this thesis.

I would also like to honor the memory of the late Professor Cees van Rhee, who, though no longer with us, played a crucial role in shaping the early stages of this research. His insights and mentorship will always be remembered and appreciated.

In the face of unforeseen circumstances, I am grateful to Professor Geert Keetels for stepping in to fill the void left by Professor Cees van Rhee's unfortunate passing. Professor Keetels' willingness to lend his expertise, encouragement, and support ensured the continuity of my academic journey.

Special thanks are extended to Cristina Panez, whose expertise and assistance in clay testing significantly enhanced the quality of this research. Her contributions played a crucial role in the experimental phase, and I am truly grateful for her collaboration.

I would also like to express my gratitude to Esmee de Quant for her invaluable assistance in designing some of the figures in this thesis. Her creativity and dedication have played a crucial role in visually communicating what is difficult to explain in words.

A personal acknowledgment is extended to Chris Snyder, my father, for his dedicated efforts in proofreading my thesis for grammar and spelling errors. His meticulous attention to detail and unwavering support have been invaluable throughout the writing process.

Finally, I would like to acknowledge the support of my family and friends, whose encouragement sustained me throughout this academic endeavor.

ABSTRACT

THIS thesis investigates the erosion process of cohesive soil due to a submerged, moving, inclined water jet. This study provides a visualization and description of the failure mechanics of cohesive soil due to a submerged inclined water jet and develops a new equation for estimating the erosion process of cohesive soil while including the angle of the water jet as a parameter. Figures providing support to this new equation are also provided in Chapter 7. The primary variables tested are jetting angle, stand-off distance, forward velocity, and jetting velocity.

The study is guided by two primary research objectives. First, to visually and descriptively understand the failure mechanics of cohesive soil subjected to a submerged inclined water jet. Second, to develop a method of predicting the erosion process of cohesive soil, considering variable jet angles, stand-off distances, forward velocity, and jet velocity of a submerged inclined water jet.

Experimental testing was conducted in the "Dredging Lab" of Delft University of Technology. The experiment involved eroding cohesive soil blocks using half of a circular nozzle placed along the wall of a flume. This nozzle configuration allowed for the nozzle to be visible during testing. I designed several half nozzles that were tested in a flume provided by TU Delft. Nozzles with a variety of nozzle diameters were designed to have either a 25^o, 45^o, 65^o, 90^o, 115^o, 135^o, or 155^o jetting angle. Seventy-two clay blocks with a known undrained shear strength were used as the cohesive test soil, allowing for immediate replacement after each test. Detailed experimental procedures are outlined in Section 5.3, offering insights into the design and execution of the tests.

The data analysis provides evidence that the jetting angle has a notable impact on the erosion process of cohesive soil. This includes a "deflecting jet" failure mode, the formation and prediction of the sediment plume, and the estimation of the erosion cavity depth. The failure mode of the soil can be seen in Section 5.5 and data analysis figures are provided in Chapter 6. Section 7.1.2 provides a new estimation for the erosion depth of cohesive soil using an inclined water jet (Equation 7.17). This study contributes to our understanding of cohesive soil erosion and methods of estimating erosion processes. The findings emphasize the crucial role of the jetting angle and provide a foundation for future research aimed at refining erosion prediction models and exploring additional parameters influencing the process. Practical applications may include improved design considerations for projects involving water jet erosion such as deep-sea mining, water injection dredging, trailing suction hopper dredgers, as well as other dredging processes involving water jetting.

Contents

NOMENCLATURE

Roman Letters

A	Surface	m^2
A_c	Activity	-
A_ω	Pore water pressure coefficient	-
c	Concentration	-
c'	Cohesion	N/m^2
c_c	Clay content, fraction of total slid mass	-
C	Compressibility	m^2/N
D	Diameter	m
e	Void ratio	-
F	Force	N
g	Gravitational constant	m/s^2
h	Drainage length	m
I	Momentum flux	N
k	Experimental constant	-
L	Length	m
LI	Liquidity index	%
LL	Liquid limit	%
m	Mass	kg
M	Momentum Force	Nm
n_0	In-situ porosity	-
N_{bc}	Bearing capacity factor	-
p	Pressure	N/m^2
PI	Plasticity index	%
PL	Plastic limit	%
q_{bc}	Bearing capacity	N/m^2
Q	Flow rate	m^3/s
r	Radial distance to centerline of the jet	m
R	Radius	m
Re	Reynolds number	-
s	Jet distance, measured along the centerline of the jet	m
su	Undrained shear strength	N/m^2
SOD	Stand off distance	m
t	Time	s
T	Temperature	^oC
u	Velocity	m/s
v	Velocity	m/s
v_t	Horizontal traverse velocity of the nozzle	m/s
V	Volume	m^3
ω	Water content in terms of mass	-
W_c	Jet cavity width	m
Z_c	Jet cavity depth	m
z	Distance in z-direction	m

Greek Letters

α	Angle	rad
α_{mom}	Entrainment coefficient	-
β	Inclination angle jet, relative to the vertical	rad
γ	Half angle at the vertex of a conical cavity	grad
δ	Boundary layer height	m
Δ	Difference between two values of a parameter	-
Δp_a	Required ambient pressure drop for cavitaion	N/m^2
ϵ	Strain	-
ζ	Auxiliary angle	rad
η	Fraction of pore water pressure that gives the effective stress	-
θ	Jetting Angle	rad
κ	Karman constant	-
μ_n	Nozzle discharge coefficient	-
ν	Kinematic viscosity coefficient	m^2/s
ρ	Density	kg/m^3
σ	Total stress	N/m^2
σ_d	Cavitation index for cone development	-
σ_{cav}	Cavitation index, defined as p_{a0}/p_j	-
σ_n	Normal stress	N/m^2
τ	Shear stresses	N/m^2
φ	Internal friction angle	grad
ω	Rotation angle of discrete soil element	rad

Subscripts	
a	Ambient
b	Bed
bc	Bearing capacity
bl	Boundary layer
d	Density
c	Critical
cav	Cavitation
ch	Characteristic
cd	Fully developed cone
cs	Critical state
cu	Curvature
dr	Flow development region
e	Erosion
ent	Entrainment
Imp	Impingement
fdc	Fully developed cone
g	Gas
gr	Granular
i	Inception
j	Jet
l	Load
ll	Liquid limit
m	Mixture
n	Nozzle
nc	Non-cavitating
out	Outer (diameter)
p	Particle
pc	Pre-consolidation
pl	Plastic limit
r	Resistant
ref	Reference
s	Solids
sk	Skeleton
sp	Specific
$stag$	Stagnation
$surf$	Surface
t	Traverse
u	Uniform
v	Vertical
$void$	Void-space (pores)
ω	Water
0	At nozzle exit or initially
∞	Infinite
$\perp$	Normal

Superscripts	
d	Deviatoric
$'$	Effective (soil pressure)

List of Figures

List of Tables

1
INTRODUCTION

1.1. BACKGROUND

DREDGING is the removal and/or transportation of material from the seabed or freshwater lake or river. There are many applications for dredging such as:

- Port and harbor maintenance and construction;
- Beach re-nourishment/Coastal protection;
- Deep-sea mining;
- Land reclamation;
- The early installation of offshore projects (oil, gas, solar, and wind farms).

This thesis was inspired by the deep-sea mining market and the search for a more environmentally compatible and efficient method of collecting polymetallic nodules. In this thesis, I will study the erosion process of cohesive soil due to a submerged, moving, inclined water jet.

Deep-sea mining entails the collection of mineral deposits from the seabed, usually at depths greater than 200 meters. These mineral deposits are typically in the form of polymetallic nodules. According to the International Union for Conservation of Nature (IUCN), there are gaps in our understanding of the deep-sea's biodiversity and ecosystem. Consequently, it is difficult to fully understand the impact of deep-sea mining. We know, however, that deep-sea mining stirs up fine sediment on the seafloor to form suspended sediment plumes. Since animals and organisms are not adapted to these sediment plumes, animals could be smothered, filter-feeding species could be harmed, and the visual communication between animals could be disrupted (**IUCN**; **2022**).

There are three types of deep-sea mining: cobalt crust mining, sulfide mining, and polymetallic nodule mining Figure 1.1. This thesis will not examine those aspects of deep-sea mining that involve the design of collectors and the process of locating a mining site. Instead, this Thesis will focus on the key process of deep-sea mining that involves the collection of polymetallic nodules. According to the International Seabed Authority, these nodules are comprised of concentric layers of manganese hydroxides and iron around a core. These nodules also consist of silicon, aluminum, nickel, copper, and cobalt among many other materials. These materials are in high demand as the world pushes for electric cars and clean energy. The polymetallic nodules vary in size but are typically between five and ten centimeters in diameter. The nodules are, generally, half buried in a sea-bottom that is mostly made up of cohesive soil. The visible surface of the nodules tends to be smoother than the surface that is buried (**International seabed authority**).

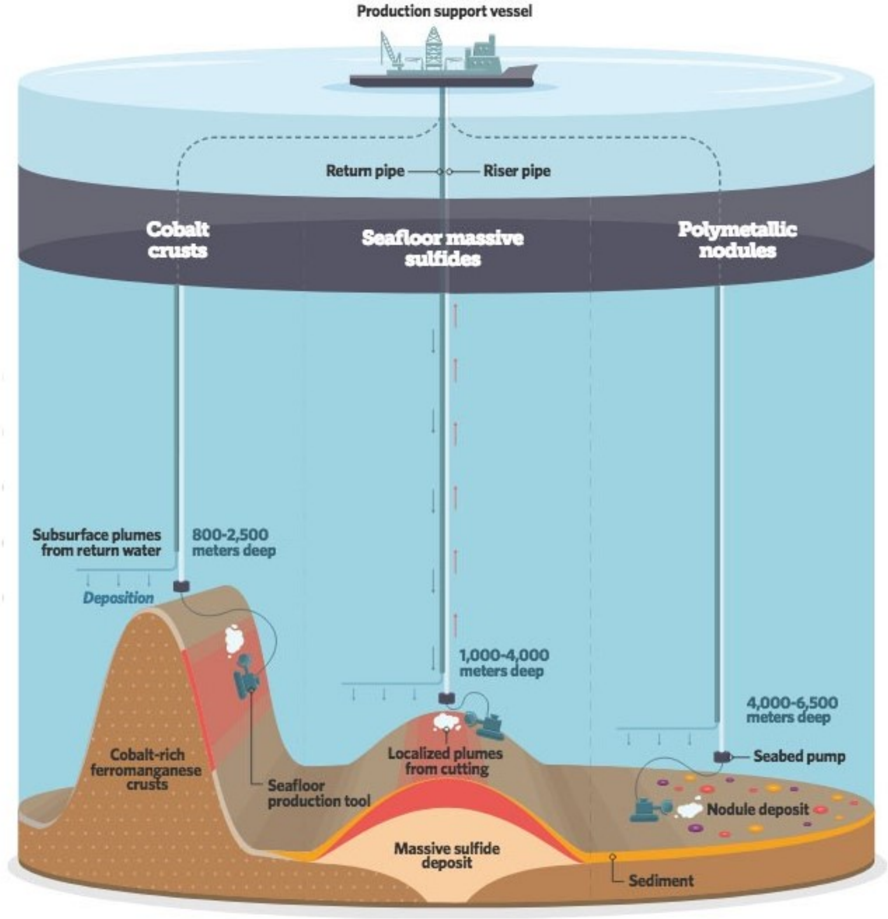

Figure 1.1: The three types of deep-sea mining (**Struck**; **2018**).

There are several ways to collect nodules, including: mechanical collection, hydraulic collection, and a hybrid collection method. According to Bedon Vasquez, the hydraulic collectors are considered more reliable and cause minimal wear to the collector (**Bedon**; **2020**). This thesis will explore a hydraulic collection method. Hydraulic dredging processes must be researched to detemine which process to pursue.

There are a few hydraulic dredging processes. One such process is "Water Injection Dredging" (WID). WID is primarily used to transport mud without having to suction the sediment and transport it manually via a suction hopper dredging vessel. WID uses a water jet suspended above the seabed to inject large amounts of water, fluidising the sediment (see Figure 1.2). The soil will then start to mobilize itself via gravity or density current down river or to a deeper area of the sea floor (**Somerset River Authority**; **2020**). The calculation for the erosion caused by WID is typically assumed to be that of a vertical water jet. However, as the dredging vessel moves the suspended water jet frequently tilts at an angle. Consequently, the calculation of erosion would be more accurate if the calculations treated the water jet as inclined rather than vertical. This is yet another reason testing the erosion process due to an *inclined* water jet may benefit the dredging industry.

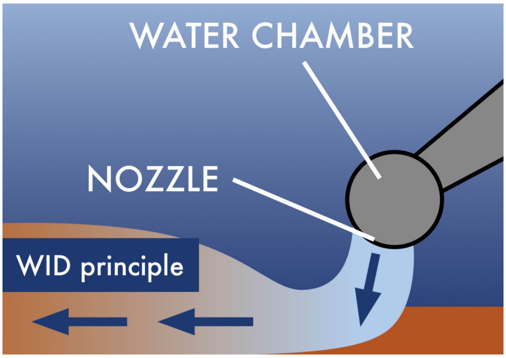

Figure 1.2: A diagram showing the principle of water injection dredging provided by **Somerset Rivers Authority (2020)**.

Inclined jetting is also used to empty the collection hoppers of a "Trailing Suction Hopper Dredger" (TSHD). Jets inserted at the bottom of the hopper are used to fluidise the sediment in the hopper, so the sediment can be removed by hydraulic transport. The fluid moves through pores in the sediment from the bottom to the surface of the hopper. The pressure difference between the bottom "high static" pressure and the surface "atmospheric" pressure initiates the flow (**Kamal**; **2017**).

Water jetting is another commonly used method to maximize the collection of sediment and typically involves fixed vertical jets on a collection head. Since the seabed is textured, fixed vertical jets are not always perpendicular to the seabed. Since this thesis explores the erosion process of an inclined jet, a fixed vertical jet is not ideal. Remarkably, inclined water jets have not been thoroughly investigated and could be a viable option for better understanding erosion (see Figure 1.3). **Liu (2023)** used inclined jets to study the effects of a "double-row hydraulic jet". However, the jet was not moving and only one nozzle diameter, $D_n = 10\,mm$, and jetting angle, $\theta = 45^o$, was tested (see Figure 1.4). In contrast, this thesis will examine this knowledge gap of using a moving inclined water jet as a hydraulic collection method while testing three nozzle diameters, six jetting angles, two stand-off distances, and four transverse velocities. I will elaborate on the details of the tests in Section 1.3.

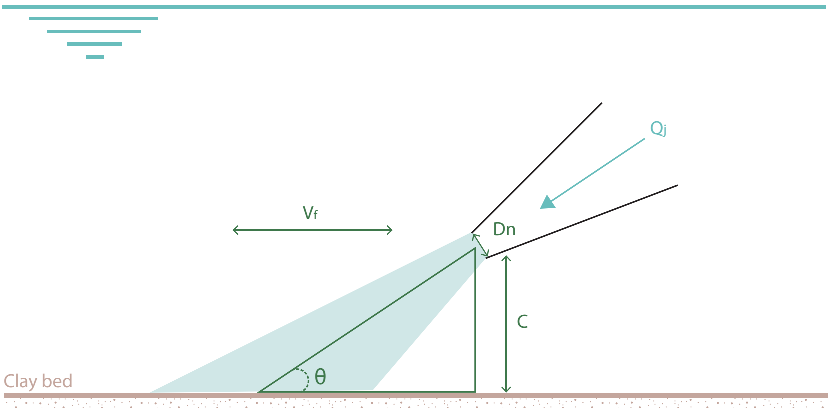

Figure 1.3: Diagram representing a submerged incline water jet. Q_j is the flow rate through the jet nozzle, v_f is the forward velocity of the collector, D_n is the nozzle diameter, C is the stand-off distance, and θ is the jetting angle.

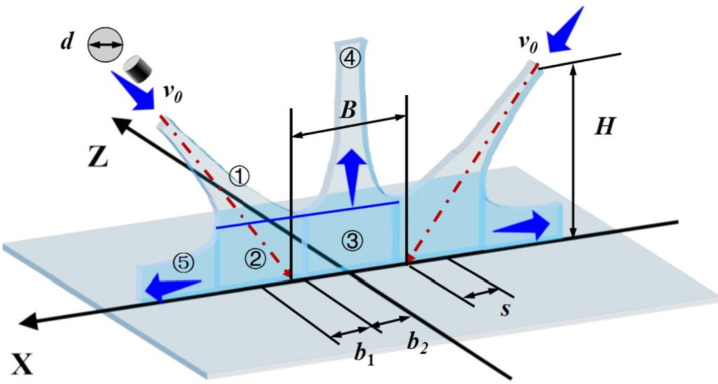

Figure 1.4: The Flow field and main parameters of the double-row water jet according to **Liu (2023)** where d = Nozzle diameter, v_0 = Velocity at the jet nozzle, b_1 = Half width of impact zone, b_2 = Half width of the upper spray formation zone, B = Target distance, H = Height from nozzle to bottom, and S = Lag point offset.

The Coandă-effect collector is an inclined water jet that utilizes water forced through a curved duct. The duct has an opening at the bottom for the collection of nodules. The Coandă-effect describes the behavior of a flowing gas or a liquid, such as water, to adhere to a surface even if that surface curves away from the initial direction of flow. The fast-moving liquid follows the curved duct and produces a low-pressure area creating a pressure gradient. The Coandă-effect collector uses this pressure gradient as a vacuum for collecting the nodules. The decreased pressure under the flowing liquid pulls the surrounding water, providing the pick-up force needed to erode the sea floor and dislodge the nodules. The nodules are then entrained in the flow of the collector and transported to the collection basin Figure 1.5. The collection process, Which focuses on nodule collection and not sediment collection, is enabled by the Coandă-effect (hence the name) (**Alhaddad**; **2023**). Figure 1.5 illustrates how the main focus of this collector it to collect the nodules and discard the sediment water mixture.

Before the experiments of **Alhaddad (2023)**, erosion was thought to be mainly caused by the flow-induced shear stress, which is shear stress caused by the flow of liquid across a surface and the shear stress value is directly proportional to the velocity of the surrounding liquid. However, after the experiments, it was found that the erosion was caused by the impingement of the flow on the seabed (**Alhaddad**; **2023**). This conclusion leads to questions about how the jetting angle will effect the erosion process.

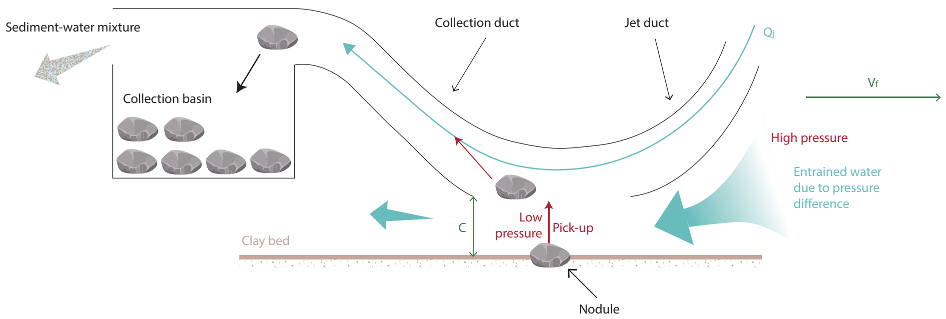

Figure 1.5: Diagram representing the Coandă-effect collector head and collection process. Q_j is the flow rate through the duct before any pick-up, Q_c is the flow rate through the duct after the pick-up of the nodules and sediment, C is the stand-off distance, and v_f is the forward velocity of the collector (**Alhaddad**; **2023**).

A moving vertical jet exerts a normal pressure equal to the stagnation pressure onto the cohesive soil. The development of the stagnation pressure derived from the jet velocity must be known to model the excavation process of a moving vertical jet in cohesive soil. This stagnation pressure is a function of the axial velocity of the jet flow and causes the soil to fail (erosion). We also know that jet velocity decreases with distance mainly due to entrainment of ambient water. There have been multiple studies on the erosion effects of vertical jets such as **Nobel (2013)**, **Wu (2018)**, **Wang (2021)**, and **Weegenaar (2015)** . However, there are few, if any, studies that investigate the impact of a submerged inclined jet in cohesive soil.

As stated in Section 1.1, assuming nodules range in size from five to ten centimeters in diameter and are partially buried in the soil, then the target erosion depth should be approximately two and a half to five centimeters since this is the approximate height out of the soil of the average nodule that is being collected. At this erosion depth, the nodules will be dislodged, and soil erosion is minimized. Sediment pick-up is minimized because only the nodules are wanted for collection and any sediment that is collected is then dumped back onto the seafloor covering anything that may be on the surface of the seabed. This thesis will study how altering the jetting angle of the nozzles, jetting velocity, and/or stand-off distance can optimize the pick-up of these nodules while reducing the pick-up of sediment.

Arnold Nobel developed a 1D-approach to predict the jet cavity dimensions (depth and width) as a function of the vertical jet parameters and soil properties (**Nobel**; **2013**). In this 1D-approach, the stagnation pressure is derived from the jet velocity, which is obtained by solving the mass and momentum balance. However, this approach does not account for the angle of the jet.

Using an inclined jet, the dynamic pressure is utilized since there is both a vertical and horizontal force on the clay. A vertical jet creates only a stagnation pressure.

Erosion of submerged cohesive soil by water jets is a complex process involving various factors, including the properties of the soil, water, and the characteristics of the jet. To understand this process comprehensively, The following factors are considered:

- Soil Properties:
  The erosion of cohesive soil depends on factors such as cohesion, particle size distribution, plasticity, and shear strength.
- Erosion Mechanism:
  Soil erosion due to a water jet occurs due to the impact and shear forces of the water jet. The water jet creates channels/craters in the clay by dislodging soil particles and carrying them away.
- Jet Characteristics:
  The nozzle diameter, jetting velocity, and angle of jetting are all key parameters of the water jet. These parameters will determine the intensity and impact energy of the jet.
- Undrained shear strength:
  The undrained shear strength of cohesive soil, s_u, defines the soil's resistance to shearing under undrained conditions.
- Dynamic Pressure:
  The dynamic pressure, P_d, of the water jet is a measure of the kinetic energy of the jet and is related to the jetting velocity. The dynamic pressure is used to estimate the erosion potential.

- Erosion Depth:
  The erosion depth, Z_c, is the measure of soil removed by the water jet. This is influenced by the s_u, P_d, and other factors. Erosion is still not fully understood theoretically and so empirical relationships are used to estimate the erosion depth.

- Erosion Rate:
  The erosion rate, ε, is the volume of soil eroded per unit time. One can solve for erosion rate by multiplying the erosion depth by the cross-sectional area of the water jet and then dividing by the time it takes to reach the target erosion depth.

- Laboratory Testing:
  Tests such as triaxial tests, can be used to determine soil properties like the undrained shear strength. Laboratory tests can be used to ensure accurate results and confirm calculated data.

1.2. OBJECTIVE

THE objective of this thesis is to study the erosion of cohesive soil, such as clay, due to a submerged, moving inclined water jet. This information can be used to contribute to the 1D model created by Arnold Nobel (**Nobel**; **2013**) by including the angle of the submerged water jet as a changeable variable to aid in optimizing the collection of nodules under various environmental conditions. The more information about the erosion process of cohesive soil, the more efficient we can make the dredging process. This knowledge will benefit the dredging industry in general.

Water jetting is used to create a low-pressure zone below the collector creating a vacuum that dislodges the nodules from the cohesive soil allowing them to be collected. As a part of this process, the entrained water moving from high pressure to low pressure and the "pick-up" force on the nodules also effects the soil around the nodules resulting in suspended sediment. That suspended sediment is collected as a by-catch of the nodules and then released back into the environment as a sediment plume. This plume settles over and covers organic matter on the sea-bottom. This thesis will investigate the effects "jetting angle", "jetting velocity", and "stand-off distance" have on the erosion process of cohesive soil using a submerged inclined water jet. Using the data collected during this thesis, mining companies using hydraulic collection methods may optimize their collection of nodules while reducing suspended sediment.

Research objectives:

- To visualize and describe failure mechanics of cohesive soil due to a submerged inclined water jet.

- To develop a method for predicting the erosion process of cohesive soil from variable jet angles, stand-off distances, forward velocity, and jet velocity of a submerged inclined water jet.

- To contribute to the 1D-approach of Arnold Nobel's research by including the angle of the water jet as a parameter that will affect the jet cavity dimensions.

1.3. METHODOLOGY

THE most effective way of pursuing the aforementioned objectives is through experimental lab tests. Experiments will allow me to not only collect data from measurements but also to collect visual data from videos that measurements are unable to collect. The visual data will bring about a better understanding of what happens during the erosion process. Researching previous work on this subject will aid in determining the best coarse of action for conducting the lab tests. The theses of **Nobel (2013)**, **Wu (2018)**, **Wang (2021)**, and **Liu (2023)**, considered with other papers cited throughout this study, will be referenced frequently, since they are the most recent studies done on water jets and clay.

Cohesive soil, with a thickness of 13 centimeters, will be placed in the middle of a flume. This thickness will ensure adequate clearance from the bottom of the test flume and make the testing easily visible. The sediment used in this experiment will have a "Eurocode 7" classification of "very low" undrained shear strength which ranges from 10-30 kPa (**Townend**; **2011**). A sediment with an undrained shear strength in the range of 20-30 kPa will be used to enable clear visualization of the testing. A more detailed explanation of how this will be achieved is stated in Section 2.1.

The main difference between the tested sediment and the sea floor will be the absence of organic matter in the tested sediment and the undrained shear strength. Lacking in organic matter will not have a significant effect on the objective of the experiment since the undrained shear strength of the soil will be the the most important property of the clay as will be explained in Chapter 2.

A submerged inclined water jet will pass over the soil in one direction at various nozzle diameters (12, 17, 20 mm), jetting angles (25, 45, 65, 115, 135, and 155 deg.), stand-off distances (5 and 10 cm), forward velocities ranging from 0.15-0.6 m/s, and jetting velocities (10 - 13 m/s). Due to the slow settling rate of the particles, multiple blocks of clay are necessary (72 blocks), so that I can shorten the interval between each pass. Instead of having to wait for sediment particles to settle, I can drain the water immediately after the test and replace the used clay block with a new block and start a new test. Each block of clay will be used for two passes of the jet, one on each side of the section. Two passes on each block will reduce the number of clay blocks necessary to complete the tests. The jet will be attached to a rail system specifically designed by the TU Delft lab technicians to fit the small flume. Details of the experiment procedure can be found in Section 5.3.

1.4. OUTLINE OF THESIS

THIS thesis will consist first of literature reviews of cohesive sediment, erosion due to submerged inclined water jets, and previous relevant experiments. I will detail the set-up for my experiment and my objective after the literature review. Details will consist of information such as the dimensions of the flume being provided (300 cm long x 20 cm wide x 40 cm high) as well as the properties of the cohesive soil used and the physical properties of the water jet (such as: nozzle diameters, D_n, of 12, 17, and 20 mm; the jetting angle, θ, 25, 45, 65, 115, 135, and 155 degrees (while using 90 degrees as a control angle); and stand-off distance, SOD, 5 and 10 cm). I will then discuss the findings of my experiment and provide my conclusions and recommendations for further work in the field.

This thesis will be limited to fully saturated homogenous cohesive soil with the following properties: brown clay made up of mostly Illite and a undrained shear strength ranging from 10-30 kPa. The soil will be exposed to a submerged inclined water jet moving in one direction.

2

Cohesive Soil

2.1. Introduction

Cohesive soil is typically a mixture of clay, sand, and silt where the clay particles are dominant in the soil and are primarily responsible for the cohesive behavior of the soil. One must understand the properties of the soil in question to understand how to investigate the erosion process of cohesive soil.

The main characteristics of cohesive soils, such as brown clay, are:

- High water content
- Highly compressible
- Moderate-to-high plasticity
- Low strength
- Very low water permeability.

Since cohesive soil has low water permeability and is highly compressible, water mixed within the soil will not drain when the soil is compressed. Therefore, there is an "undrained response" to the force exerted on the cohesive soil. This undrained response allows us to classify the soil strength using the undrained shear strength (s_u).

Using the cohesion (c'); effective compressive normal stress on the shear plane ($\sigma'_\perp$); and the internal friction angle (φ); we can determine the shear strength (τ) of the soil using the Mohr-Coulomb law equation:

$$\tau = c' + \sigma'_\perp * tan(\varphi) \quad (2.1)$$

According to **Terzaghi (1943)**, the effective compressive normal stress can be calculated by taking the total compressive normal stress ($\sigma_\perp$) minus the pore water pressure (p_w) of the soil:

$$\sigma'_\perp = \sigma_\perp - p_w \tag{2.2}$$

2

The internal friction angle (φ) depends on multiple parameters and contributes to the sliding resistance between the soil particles (**Rowe**; **1962**). The parameters that have the largest effect on the internal friction angle are: the clay content (c_c which is the mass of the clay particle divided by the total mass of the soil particles), the chemical properties of the pore water, the internal structure of the clay, and the consolidation ratio. The internal friction angle of normally consolidated cohesive soils range from 20^o to 25^o. As a general rule: the higher clay content(c_c), the lower water permeability (k_w), the greater the compressibility (C), the lower the internal friction angle (φ), and the greater plasticity (PI) (**Nobel**; **2013**).

2.2. CLASSIFICATIONS

SOIL is generally described using four labels: gravel, sand, silt, and clay. The difference between these soil types is their particle/grain size. According to the Unified Soil Classification System (USCS), which can be seen in Figure 2.1, and the Dutch classification system (NEN), if the soil is comprised of more than 50%, by weight, of gravel and sand, the soil is classified as "coarse grained", "granular", and "cohesion-less". If the soil contains over 50% by weight of silt and clay, then the soil is classified as "fine grained" and "cohesive". This study will focus on cohesive soil.

Table 2.1: The particle size distribution according to USCS and NEN, where D_p is the particle diameter in mm (**Nobel**; **2013**).

Soil	**USCS**	**NEN**
Gravel	$D_p > 4.75$	$D_p > 2$
Sand	$4.75 > D_p > 0.075$	$2 > D_p > 0.063$
Silt	$0.075 > D_p > 0.005$	$0.063 > D_p > 0.002$
Clay	$0.005 > D_p$	$0.002 > D_p$

UNIFIED SOIL CLASSIFICATION AND SYMBOL CHART		
COARSE-GRAINED SOILS (more than 50% of material is larger than No. 200 sieve size.)		
GRAVELS More than 50% of coarse fraction larger than No. 4 sieve size	Clean Gravels (Less than 5% fines)	
	GW	Well-graded gravels, gravel-sand mixtures, little or no fines
	GP	Poorly-graded gravels, gravel-sand mixtures, little or no fines
	Gravels with fines (More than 12% fines)	
	GM	Silty gravels, gravel-sand-silt mixtures
	GC	Clayey gravels, gravel-sand-clay mixtures
SANDS 50% or more of coarse fraction smaller than No. 4 sieve size	Clean Sands (Less than 5% fines)	
	SW	Well-graded sands, gravelly sands, little or no fines
	SP	Poorly graded sands, gravelly sands, little or no fines
	Sands with fines (More than 12% fines)	
	SM	Silty sands, sand-silt mixtures
	SC	Clayey sands, sand-clay mixtures
FINE-GRAINED SOILS (50% or more of material is smaller than No. 200 sieve size.)		
SILTS AND CLAYS Liquid limit less than 50%	ML	Inorganic silts and very fine sands, rock flour, silty of clayey fine sands or clayey silts with slight plasticity
	CL	Inorganic clays of low to medium plasticity, gravelly clays, sandy clays, silty clays, lean clays
	OL	Organic silts and organic silty clays of low plasticity
SILTS AND CLAYS Liquid limit 50% or greater	MH	Inorganic silts, micaceous or diatomaceous fine sandy or silty soils, elastic silts
	CH	Inorganic clays of high plasticity, fat clays
	OH	Organic clays of medium to high plasticity, organic silts
HIGHLY ORGANIC SOILS	PT	Peat and other highly organic soils

LABORATORY CLASSIFICATION CRITERIA		
GW	$C_u = \frac{D_{60}}{D_{10}}$ greater than 4; $C_c = \frac{D_{30}}{D_{10} \times D_{60}}$ between 1 and 3	
GP	Not meeting all gradation requirements for GW	
GM	Atterberg limits below "A" line or P.I. less than 4	Above "A" line with P.I. between 4 and 7 are borderline cases requiring use of dual symbols
GC	Atterberg limits above "A" line with P.I. greater than 7	
SW	$C_u = \frac{D_{60}}{D_{10}}$ greater than 4; $C_c = \frac{D_{30}}{D_{10} \times D_{60}}$ between 1 and 3	
SP	Not meeting all gradation requirements for GW	
SM	Atterberg limits below "A" line or P.I. less than 4	Limits plotting in shaded zone with P.I. between 4 and 7 are borderline cases requiring use of dual symbols.
SC	Atterberg limits above "A" line with P.I. greater than 7	

Determine percentages of sand and gravel from grain-size curve. Depending on percentage of fines (fraction smaller than No. 200 sieve size), coarse-grained soils are classified as follows:

Less than 5 percent .... GW, GP, SW, SP
More than 12 percent .... GM, GC, SM, SC
5 to 12 percent .... Borderline cases requiring dual symbols

Figure 2.1: Unified Soil Classification System (USCS).

The meanings of the primary and the secondary descriptive letters are as follows:

2

Table 2.2: The descriptive letters used in the USCS.

Primary Letters	Secondary Letters
G: Gravel	W: Well Graded
S: Sand	P: Poorly Graded
M: Silt	M: Non-Plastic Fines
C: Clay	C: Plastic Fines
O: Organic	L: Low Plasticity
Pt: Peat	H: High Plasticity

2.3. PLASTICITY

THE lowest water content at which the soil does not change volume and does not crack is known as the "plastic limit" (PL). This water content (ω) is the boundary between the solid and plastic state of the soil. The water content is the ratio of the water mass to the mass of the solids in the soil sample. The water content boundary between the plastic and the liquid state of the soil is called the "liquid limit" (LL). These limits are also known as the "Atterberg limits," which are frequently used for identifying and classifying cohesive soil. The higher the liquid limit, the greater capacity the soil has to bind pore water. This capacity to bind pore water is a function of specific surface area (A_s). One may calculate the liquid limit by the following equation (**Farrar and Coleman**; **1967**):

$$LL = 19 + 0.56 * A_s \tag{2.3}$$

The difference between the liquid limit and the plastic limit is known as the "plasticity index" (PI):

$$PI = LL - PL \tag{2.4}$$

where: the higher the plasticity index, the more compressible the soil and the more the volume changes when the soil is loaded and unloaded. The USCS plotted the plasticity index as a function of the liquid limit, and can be seen in Figure 2.2 bellow:

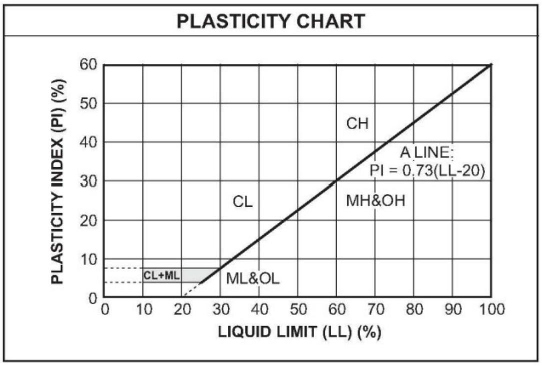

Figure 2.2: Unified Soil Classification System (USCS) Plasticity chart.

The "A-Line" portrayed in Figure 2.2 separates and distinguishes between the inorganic clays and soils (above) and the organic and silt rich soils (below). If one was to draw a vertical line from a liquid limit of 50%, everything to the left of that line would be considered "low plastic" and everything to the right of that line would be considered "high plastic".

2

The number and type of clay particles will influence the plasticity of the soil sample. Finding the activity (A_c) of the soil can help distinguish between types of clay:

$$A_c = \frac{PI}{c_c} \tag{2.5}$$

where c_c is the clay content and equals $\% < 2\,\mu m$.

The activity of the soil relates to the ability of the clay particles to isolate the non-clay particles. Isolation prevents the non-clay particles from forming a non-clay skeleton.

The liquid index (LI) is used for comparing the consistencies of different cohesive soil. A soil with a liquid index greater than "one" is considered to be a fluid. A soil with a liquid index of less than "zero" is considered to be a non-plastic granular soil. The liquid index can be calculated as:

$$LI = \frac{\omega - PL}{PI} \tag{2.6}$$

2.4. SOIL SKELETON

THE skeleton of the soil has a significant influence on the behavior of the soil. A clay-skeleton typically has a higher compressibility than a granular-skeleton and the relative partical movement in a granular-skeleton is more constrained (**Winterwerp**; **2004**). The more constrained movement is a result of the stiffness and the shape of the soil particles.

The "actual void ratio" is used to help classify the soil skeleton and is defined as the volume of the pores between particles divided by the volume of the specific particles. When a granular-skeleton exceeds its maximum void ratio ($e_{gr,max}$), the particles will be isolated in a clay-water mixture. This will result in an increase of compressibility of the skeleton and the mobility of the particles (**Nobel**; **2013**).

The minimum clay content (c_c) of a clay-skeleton dominated soil for any water content (ω) can be calculated using the following equation:

$$c_c > \frac{e_{gr,max}}{1+e_{gr,max}} - \frac{\omega}{1+e_{gr,max}} * \frac{\rho_s}{\rho_\omega} \tag{2.7}$$

2

with the following assumptions:

- the soil is fully saturated;
- all of the pore water is associated with the clay phase; and
- the specific density (ρ_s) of the clay and granular particles are equal.

Using this relation for a water content of 0.25 and a maximum granular particle void ratio of 0.9, just 13% of the total solid mass must be clay to prevent the granular particles from having direct contact between them (**Nobel**; **2013**). This percentage relates well to the critical clay content of 15% between cohesive and non-cohesive soils as determined by **Skempton (1985)**.

2.5. CLAY

According to **Mitchell and Soga (2005)**, deep-ocean deposits consist primarily of brown clays and calcareous and silicious oozes, ranging from 300 to 600 meters thick. About 60% of the particles are finer than 60 μm, and the clay is made up of Chlorite, Smectite, Illite, and Kaolinite. It is also noted that Illite is often the most abundant component. Clay is typically composed of aluminum/magnesium octahedral-sheets and silica-sheets made of silica tetrahedra. The most common clay materials are Kaolinite, Montmorillonite and Illite. Knowing the composition of the brown clay I am interested in enables me to use the following data from **Mitchell and Soga (2005)** (Table 2.3).

Table 2.3: The properties of Illite, Kaolinite, Chlorite, and Smectite documented by Mitchell and Soga (2005). (**Mitchell and Soga**; **2005**)

Properties	**Illite**	**Kaolinite**	**Chlorite**	**Smectite**
Liquid Limit (%)	60 - 120	30 - 110	44 - 47	-
Plastic Limit (%)	35 - 60	25 - 40	36 - 40	-
Shrinkage Limit (%)	15 - 17	25 - 29	-	-
Activity ($-$)	0.5 - 1	0.5	-	1 - 7
Particle Size (μm)	0.003 - 0.1 x < 10	0.1 - 4 x 0.05 - 2	-	-
Specific Surface Area (m^2/g)	80 ± 20	15 ± 5	-	-
Specific Density (kg/m^3)	2800 ± 200	2670 ± 10	-	-

Since brown clay is mostly composed of Illite, it is important to understand the properties of Illite. Mitchell and Soga explain that the basal layer of Illite is very similar to that of Montmorillonite, which consists of one aluminum octahedral sheet between two silica tetrahedral sheets (2:1). Mitchell and Soga provide an illustration of Illite's composition Figure 2.3 (**Mitchell and Soga**; **2005**):

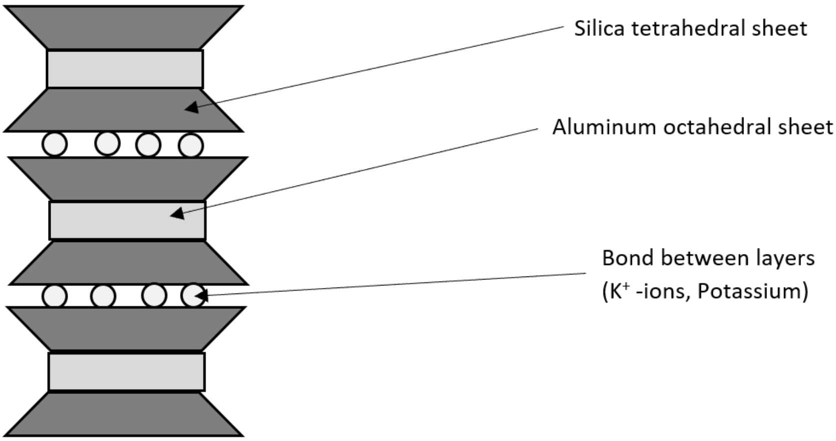

Figure 2.3: The basal layer formation of Illite according to **Mitchell and Soga (2005)**.

Clay must be considered a variable in this thesis due to the potential for human error while making the clay for testing. A clay mixture used in **Ghiabi (2007)** that has a natural water content of 15% is an option. The particle size analysis showed that the fine-grained soil contained 40% clay fraction ($< 0.002\ mm$), 52% silt, and 8% sand. The liquid limit of this clay was 25% and the plastic limit was 15%. The activity of the clay was estimated at 0.25. Using the equation $C_u = k\alpha * \frac{Q}{h^2}$ (Hansbo's equation) the undrained shear strength of the clay is estimated to be 2.63 kN/m^2 (kPa) (moisture content near 26%). The means of making this clay mixture is presented in **Ghiabi (2007)**.

The preferable option would be "Artificial Clarion-Clipperton Zone" (ACCZ) clay. The ACCZ clay consists of two materials: 1) Sibelco FT-S1 (Abidichte Ton), which is composed of 64% kaolinite, 10% Illite, 19% quartz, and 7% other minerals; and 2) Cebo OMCA Betonite, which is composed of 17% kaolinite, 17% Illite, and 66% montmorillonite (**Enthoven**; **2021**). This material is often used as a substitute for deep-sea sediment and is made to mimic the mechanical strength of the Clarion-Clipperton Zone (CCZ) clay. According to **Boschen-Rose (2020)** the undrained shear strength of the soil found in the CCZ with nodules half imbedded in the soil was a range of 0 - 7 kN/m^2 (kPa). The range at the Blue Nodules field test site (with no nodules) was 0 - 14 kN/m^2 (kPa).

Unfortunately, ACCZ clay is not available for this thesis. Therefore, I will use "Kaolin" clay suggested by the department of geoscience and engineering at TU Delft. The Kaolin clay should have similar properties to the ACCZ clay such as the material and the undrained shear strength; however, the undrained shear strength will be higher than preferred. A triaxial shear test will be preformed to determine the actual undrained shear strength of the test clay.

2

2.6. Triaxial Shear Test

A triaxial shear test will be preformed to determine the undrained shear strength (s_u) of the clay. It is important that the undrained shear strength is known because this will affect the jetting velocity and jet pressure needed to erode the clay sample. Since a goal of this study is to examine clay erosion due to a submerged inclined water jet, the parameters must be set so that erosion is clear and the erosion process is visible.

"Triaxial testing" is a form of shear test for soils while the soil sample is under confining pressure. This pressure is designed to simulate stresses from surrounding soil. The purpose of triaxial testing is to measure the shear strength of the soil in question at different drainage conditions (**Backus**; **2021**). For this study, since I am working with fully submerged clay, the test will be conducted for "undrained" conditions. "Undrained" conditions means that the pore water is unable to drain out of the soil during loading.

There are three types of conventional triaxial tests for cohesive or free-draining soils: Unconsolidated Undrained (UU), Consolidated Undrained (CU), and Consolidated Drained (CD). Each of these test methods will refer to different sample types that can be used for each test (**Backus**; **2021**):

- Intact soil: A sample that is removed directly from its native location, making sure not to change or affect the content, structure, or moisture of the soil. This type of sample is commonly referred to as an "undisturbed sample".
- Remolded soil: A sample that is molded from deconstructed soil to a desired shape for testing, but which maintains the moisture and density of the soil. This method is often used when a natural cohesive soil sample contains large particles that one wants to remove.
- Compacted/Reconstituted soil: A sample that is compacted into a mold to form a test sample. A reconstituted sample is compacted to a specific density and moisture for testing.

2.6.1. Unconsolidated Undrained

Also known as the "Q," or "quick-test", the UU Triaxial Compression Test on cohesive soils can be used when soil samples are intact, compacted, or remolded. No drainage occurs during the consolidation and shear phases of the tests and the sample may not be 100% saturated. The loads are applied quickly. Theoretically, the sample is not consolidated and pore pressures are not normally measured. This type of test is mainly intended for soils with a very low permeability rate (**Backus**; **2021**).

2.6.2. CONSOLIDATED UNDRAINED

In the CU Triaxial Compression Test for cohesive soils (the "R" test), drainage is allowed during the consolidation phase, which will allow for volume change. Drainage is not permitted during axial loading. The soil sample must be fully saturated for the R-test (**Backus**; **2021**). In the R-test, one measures the axial load, deformation, and pore pressure. These characteristics will be used to determine the total stresses and axial compression of the sample.

2.6.3. CONSOLIDATED DRAINED

The CD Triaxial Compression Test for soils is known as the "S," or slow test. The S-test is most suitable for free-draining soils. In the S-test, drainage is allowed in the consolidation and shear phases. Consequently, there is no excess pore pressure at shear failure. This test can be used when the soil samples are intact or reconstituted. Measurements of the axial load and deformation, as well as volumetric changes, are used to calculate the principal stresses. The S-test may take weeks if cohesive soils are used (**Backus**; **2021**).

2.6.4. SAMPLE TESTING

For this study, a CU Triaxial Compression Test was conducted with the help of Cristina Cavero Panez, of the Department of Geoscience and Engineering (GSE) at TU Delft. Before we conducted the test, we trimmed a sample of the clay for testing to a $35x82\ mm$ cylinder sample with a weight of $184.48\ g$. The sample's size had to be as uniform as possible for the CU test to yield an accurate result. Three measurements were made at the top, middle, and bottom of the sample to ensure that the sample was uniform. The measurements for the sample can be seen in Table 2.4 and images of this process can be seen in the following Figures (Figure 2.4-Figure 2.5):

Table 2.4: Clay sample measurements after trimming.

Top Diameter (mm)	**Middle Diameter** (mm)	**Bottom Diameter** (mm)
37	38	39
37.5	38	38.5
37.2	38	39.2

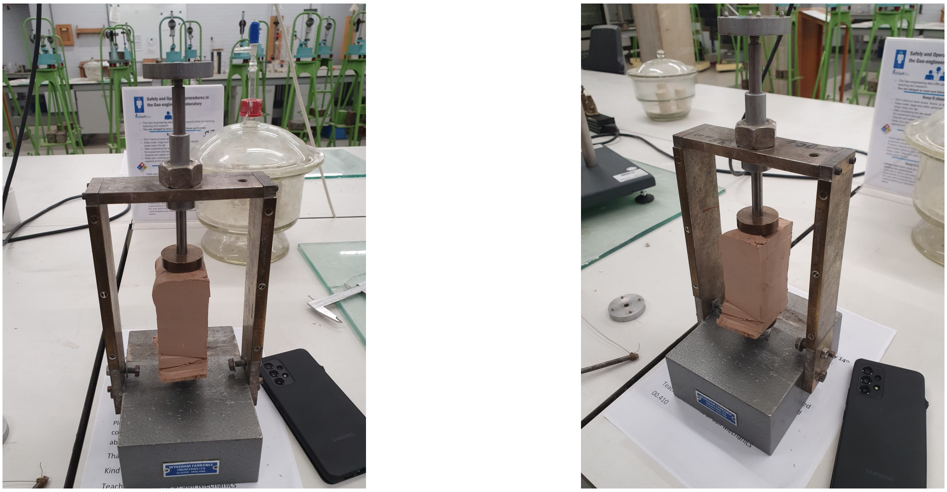

Figure 2.4: Pre-trimmed clay sample in the trimming rig designed to create a test sample with even dimensions all around.

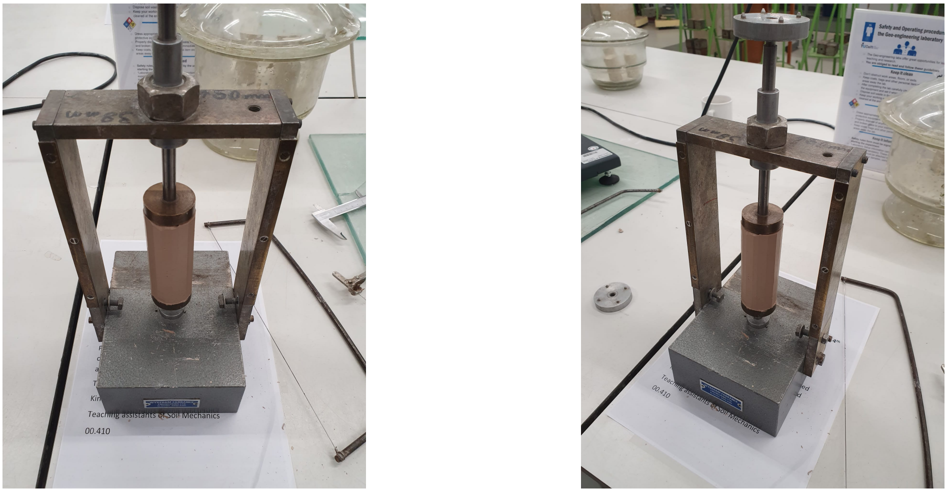

Figure 2.5: Trimmed, uniform clay sample in the trimming rig ready to be teststed. See the post-trimmed dimentions in Table 2.4.

Since we are using a CU test, the sample must be saturated to remove any trapped air. Saturation will take about 2.5 hours, after which we are able to start the consolidation stage of the test. This stage of the test can be seen in the figures below (Figure 2.6-Figure 2.7):

Figure 2.6: Post-trimmed clay sample placed in a non-permeable membrane and attached to the CU testing rig.

Figure 2.7: CU test, Saturation stage: Test sample is encased in pressure controlled container and saturated with water until there is no air left in the sample.

Because we are conducting a CU test on cohesive soil, the test took a time span of approximately three weeks under the watch of Cristina Panez. During the three week interval, we determined the water content of the clay using some of the extra clay pieces (Table 2.5):

Table 2.5: Water content of clay.

Water Content	
	Weight (g)
Container	35.69
Container + wet sample	64.21
Container + dried sample	58.53
Water content	25%

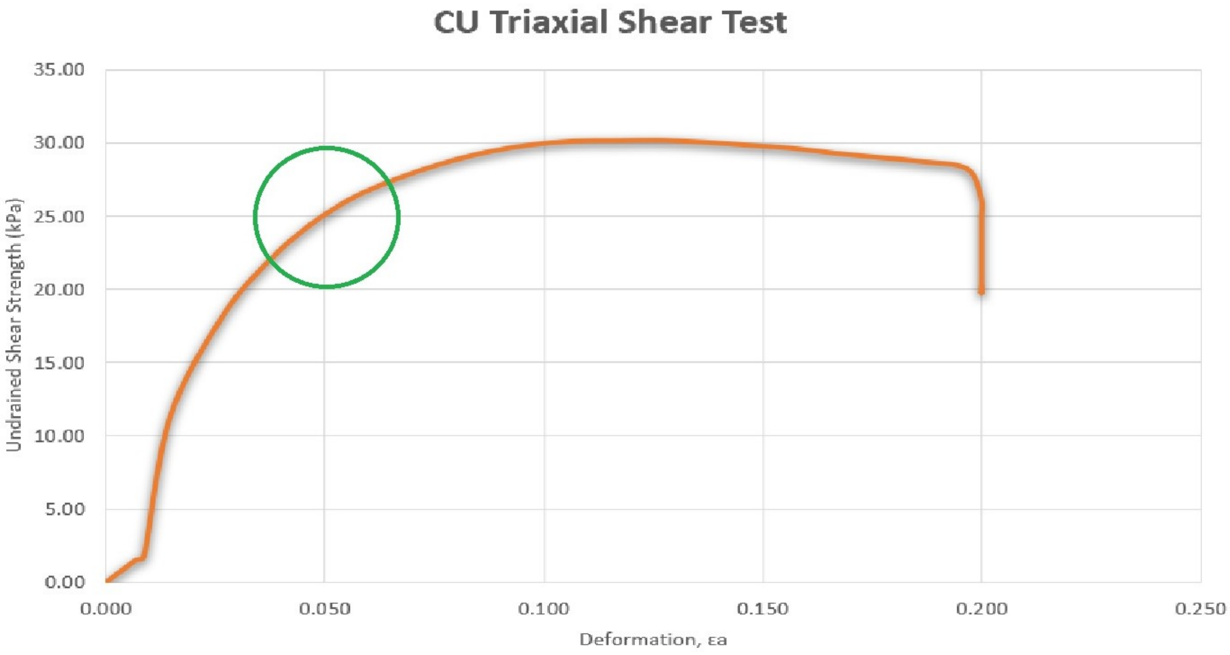

Figure 2.8: The results of our CU Triaxial Shear Test with the determined range for the undrained shear strength marked with a circle (20 to 30 kPa).

The conclusion of the CU Triaxial Compression Test is illustrated in Figure 2.8.The undrained shear strength wato be in s found the range of 20 to 30 kPa. To determine this range we observed the peak of the curve to be at 30kPa and since clay does not fail rapidly, Cristina Panez suggested that I use a range starting at 20 kPa, and so to simplify calculations, we agreed to use an undrained shear strength of 25 kPa.

2

2.7. BULK EROSION

BULK erosion is typically discussed when eroding cohesive soil. Soil particles in cohesive soil are very small and compact. The soil volume remains restrained because the pore water slows the change in soil volume, which delays the increase in volume and the decrease of the mean effective stress. Consequently, the time necessary for water to be drawn into the cohesive soil as it swells and begins to erode is too long to be characterized as fast erosion. Maintaining the effective stress preserves the effective strength of the soils and thereby increases resistance to surface erosion. Greater momentum leads to bulk erosion or soil deformation (**Nobel**; **2013**).

Bulk erosion occurs when shear surfaces form and the shear stresses along these surfaces are equal to the undrained shear strength of the cohesive soil (s_u). When the load created by a water jet is greater than the shear stresses, the soil will fail (erode). Considering a vertical jet and a flat horizontal soil surface, one must acknowledge vertical loads and a shear resistance termed "bearing capacity" (q_{bc}). The bearing capacity for a circular load at the soil surface is calculated using the following equation (**Nobel**; **2013**):

$$q_{bc} = N_{bc} * s_u \approx 6.2 * s_u \tag{2.8}$$

where N_{bc} is the bearing capacity factor. The bearing capacity factor will decrease when the soil surface is not completely flat. In theory, N_{bc} could decrease to a value as low as two. For this study, the jet will be at an incline. So, the bearing capacity factor can be treated as if the soil surface is not completely flat but at an angle.

The criterion for undrained soil failure is defined as:

$$p_{stag} > 2 \sim 6.2 * s_u \tag{2.9}$$

where the normal stresses induced by turbulent flow scale with the stagnation pressure and can be defined as (**Nobel**; **2013**):

$$p_{stag} = \frac{\rho_m * u_u^2}{2} \tag{2.10}$$

where ρ_m is the density of the jet flow and u_u is the mean velocity in the jet. p_{stag} will be discussed further in Chapter 3.

2.8. CLAY PREPARATIONS

THE 72 clay blocks that will be used during the experiments were ordered from the company "Keramikos", as recommended by the Department of Geoscience and Engineering at TU Delft. A Consolidated Undrained Triaxial Compression Test, determined the undrained shear strength of the clay to be 25 kPa (Section 2.6.4). The components of the clay are detailed in Table 2.6, Table 2.7, and Table 2.8.

2

Table 2.6: The chemical analysis of the Kaolin clay supply (%): (**Kaolin**; **2021**)

Component	Typical	Warranty
SiO_2	47.5	-
AL_2O_3	36.9	> 36.0
Fe_2O_3	0.90	< 0.95
TiO_2	0.23	< 0.30
MgO	0.35	-
CaO	0.23	-
K_2O	0.90	< 1.20
Na_2O	0.05	-
LOI	12.8	-

Table 2.7: The granulometry of the kaolin clay supply (%): (**Kaolin**; **2021**)

Fraction	Typical	Warranty
$> 63\ \mu m$	< 0.01	< 0.1
$> 20\ \mu m$	1	< 5
10 - 20 μm	4	-
5 - 10 μm	10	-
2 - 5 μm	24	-
$< 2\ \mu m$	61	> 50
$D_{50}\ \mu m$	1.3	-

Table 2.8: The mineral composition of the Kaolin clay supply (%): (**Kaolin**; **2021**)

Mineralogical Composition (%): Kaolin	
Fraction	**Typical**
Kaolinite	91 ± 3
Quartz	2 ± 1
Mica Miner.	7 ± 2

2.9. SUMMARY

THIS chapter provides a thorough analysis of cohesive soil properties, classifications, plasticity, and the influence of clay in the context of erosion. Key elements include the definition of cohesive soil, its characteristics, classification systems, and the significance of parameters such as undrained shear strength and plasticity index. Additionally, the review delves into the role of clay, specifically focusing on Illite, and presents details about the triaxial shear test conducted on a Kaolin clay sample. The results indicate an undrained shear strength of approximately 25 kPa. This comprehensive overview establishes the foundation for understanding cohesive soil behavior and subsequent discussions of erosion and the experimental setup involving the prepared clay blocks.

My investigation will involve the use of cohesive soil blocks measuring $13x12.5x30\ cm$, procured in bulk from Keramikos. The consistent sourcing from a single company ensures uniformity in block composition, which is critical for maintaining the undrained shear strength of the clay samples. CU Triaxial Compression tests confirmed the clay's undrained shear strength at 25 kPa. This clay, together with three specified nozzles, will be employed in 56 tests (excluding 18 reserved for preliminary and replacement purposes). The experimental setup and procedures are detailed in Chapter 5.

3

WATER JETS

3.1. INTRODUCTION

WATER jets play an important role in dredging and deep-sea mining. Water jets are mainly used to excavate sediment from the seabed. When excavating cohesive soil, a vertical jet will exert a "normal pressure" on the soil equal to the stagnation pressure (p_{stag}), which is a function of the axial jet velocity. The pressure will cause a shear surface to form. The soil will fail along this shear surface. This form of erosion is commonly referred to as "bulk erosion" (**Nobel**; **2013**). The force exerted by the inclined jet onto the cohesive soil will be divided into a vertical and horizontal force meaning there will be no "stagnation" pressure but instead a "dynamic" pressure (P_d). This also means that the vertical force of an inclined jet will be less than the vertical force of a vertical jet. This leads to the conclusion that for a vertical and inclined jet to achieve the same result, the jetting velocity of the inclined jet must exceed that of the vertical jet. Of course, there are other factors to consider and this thesis will discover those factors and examine their contribution to the erosion of cohesive soil.

Nobel (2013) utilized the principle of Bernoulli to determine stagnation pressure. The principle of Bernoulli describes the relation between the pressure drop over the nozzle and velocity and discharge of the nozzle:

$$p_1 + \frac{1}{2} * \rho_w * u_1^2 = p_0 + \frac{1}{2} * \rho_w * u_0^2 \tag{3.1}$$

where p_1 is the pressure upstream of the nozzle, u_1 is the flow velocity upstream of the nozzle, p_0 is the pressure in the nozzle and u_0 is the exit velocity in the nozzle.

Using the definition of the pressure drop $\triangle p = p_1 - p_0$ and understanding that the velocity upstream of the nozzle is typically much less than the velocity in the nozzle, the exit velocity can be calculated as:

$$u_0 = \sqrt{\frac{2 * \triangle p}{\rho_w}} \tag{3.2}$$

Applying the principle of Bernoulli, Nobel calculated the stagnation pressure:

$$p_{stag} = \frac{\rho_m * u_u^2}{2} \tag{3.3}$$

where ρ_m is the mixture density of the jet and u_u is the jet velocity. Assuming uniform flow, jet velocity can be calculated as:

$$u_u = \frac{I}{\rho_m * Q} \tag{3.4}$$

where I is the momentum flux and Q is the jet flow rate. The uniform flow is used to simplify the calculation and is a theoretical velocity. In actuality, flow velocity will decrease with the distance to the nozzle (s), creating a velocity profile. The decrease in flow velocity is primarily due to the entrainment of ambient fluid and soil into the jet.

To test the vertical jet scenario, the nozzle is positioned at a certain distance above the original soil surface, which is referred to as the "stand-off distance" (SOD). It is important to note that the distance to the nozzle (s) is equal to the SOD in a vertical jet scenario. This is not the case when an inclined jet is used. Since the jet has a jetting angle θ, which is the angle from the original soil surface to the nozzle, where the angle is not 90^o, the distance to the nozzle can be calculated using trigonometry:

$$s = \frac{SOD}{sin(\theta)} \tag{3.5}$$

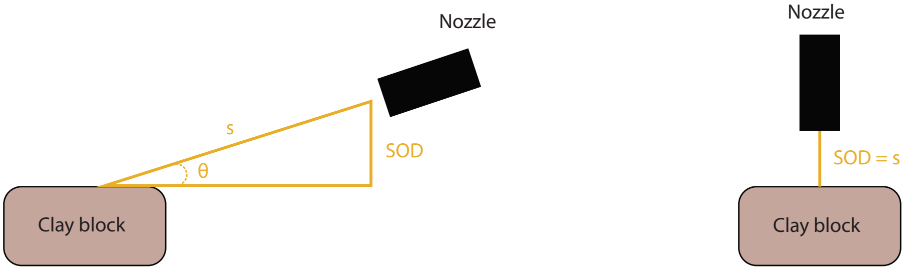

Figure 3.1: Illustration of the difference between stand-off distance (SOD) and the distance to the nozzle (s).

In **Liu (2023)**, the relationship between impact pressure and main jet parameters was obtained using "Buckingham π theorem" and equation transformation. Liu states that impact pressure at the jet impact area mainly depends on the parameters of the jet nozzle, as well as the fluid density and viscous coefficient. Since Liu maintained a constant jet angle of 45^o and the Reynolds number (Re) was large, the consideration of viscous coefficient and angle change is ignored (**Liu**; **2023**).

The impact pressure at the jet impact area, P_{imp} can be described by the following function (**Liu**; **2023**):

$$P_{imp} = f(\rho, \mu, u_u, D_n, B, SOD, n) \tag{3.6}$$

where ρ is water density, μ is dynamic viscosity, D_n is nozzle diameter, B is the target distance of the jet impact seen in Figure 1.4, SOD is the stand-off distance, and n is the nozzle group number (the number of nozzles that were used).

Liu (2023) demonstrates how the variables in Equation 3.6 can be expressed by five dimensionless equations according to π theory:

3

$$\pi = \frac{P_{imp}}{\frac{1}{2}\rho u_u^2} \tag{3.7}$$

$$\pi_1 = \frac{\mu}{\rho u_u d} = \frac{1}{Re} \tag{3.8}$$

$$\pi_2 = \frac{B}{D_n} \tag{3.9}$$

$$\pi_3 = \frac{SOD}{D_n} \tag{3.10}$$

$$\pi_4 = n \tag{3.11}$$

Now Equation 3.6 can be transformed into the following formation:

$$\pi = f(\pi_1, \pi_2, \pi_3, \pi_4) \tag{3.12}$$

$$\frac{P_{imp}}{\frac{1}{2}\rho u_u^2} = f(\frac{1}{Re}, \frac{B}{D_n}, \frac{SOD}{D_n}, n) \tag{3.13}$$

Since the nozzle is positioned at an angle, seen in Figure 3.1, I will consider the dynamic pressure instead of just stagnation pressure and will determine a new equation for erosion depth using π theory in Section 7.1.2. Dynamic pressure is closely related to kinetic energy and in some contexts, such as fluid dynamics, dynamic pressure can be used to estimate the kinetic energy of a fluid. Below are key factors of both dynamic pressure and kinetic energy:

- Dynamic Pressure (P_d):
  - Dynamic pressure is a measure of the kinetic energy per unit volume in a flowing fluid.
  - It is a measure of the pressure increase in the fluid due to its motion.
  - The formula is:
  $$P_d = \frac{1}{2} * \rho_w * u_j^2 \tag{3.14}$$
  where ρ_w is the fluid density and u_j is the fluid velocity.

3

- Kinetic Energy(KE):
  - Kinetic energy is a measure of the energy of an object or a fluid particle in motion.
  - It is defined as:

$$KE = \frac{1}{2} * m * V^2 \tag{3.15}$$

    where m is the mass of the object or particle and V is the velocity.
  - Kinetic energy is a more general concept that can apply to any moving object, not just fluids.
  - while dynamic pressure relates specifically to fluid flow, kinetic energy applies to all forms of motion.

Since $m = \rho * A * V$, I can substitute this into the kinetic energy equation:

$$KE = \frac{1}{2} * \rho * A * V^2 \tag{3.16}$$

The concepts above are based on the conservation of energy and the principles of fluid dynamics (**Fluid Mechanics**; **1990** and **Fundamentals of Physics**; **2013**). The dynamic pressure and the kinetic energy equations are not equivalent because they use different factors. However, in the context of water jet erosion, the dynamic pressure is often used to represent the kinetic energy of the water jet impacting a surface. An example of this representation can be seen in Bernoulli's equation:

$$P + \frac{1}{2} * \rho_w * u_j^2 + \rho * g * h = constant \tag{3.17}$$

Bernoulli's equation relates the pressure, velocity, and potential energy of a fluid in steady, incompressible flow along a streamline. $\frac{1}{2}\rho u_j^2$ in Equation 3.17 is the equation for dynamic pressure and is essentially the kinetic energy per unit volume of the fluid due to its motion.

This ability to substitute dynamic pressure for kinetic energy will be utilized in Section 7.1.2, as well as a detailed explanation on how to predict the erosion depth.

3.2. FLOW FIELD AND DEVELOPMENT

Figure 3.2, provided by Nobel, illustrates the flow field of a fully submerged free circular jet. The jet velocity at the nozzle exit is assumed to be uniform (u_0). Uniform jet velocity is assumed since the hindrance of the mixing layer, which is at the interface between the jet and ambient water, increases with the distance to the nozzle. Consequently, when the distance is zero (at the nozzle exit) the mixing layer is negligible. This region from the nozzle exit to the point where the turbulence of the mixing layer reaches the axis is called the "potential core". The region past the potential core is fully developed flow and the potential core has disappeared.

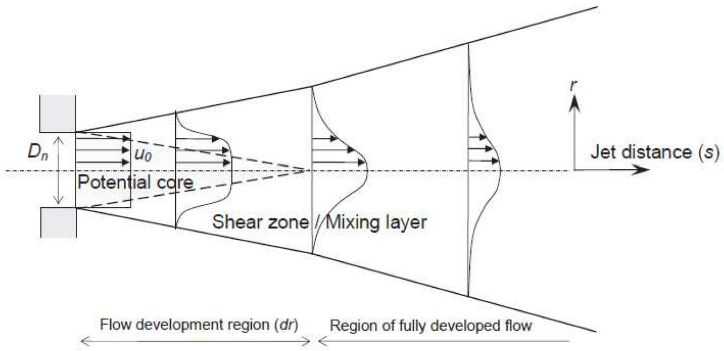

Figure 3.2: The flow field of a free circular jet fully submerged in water as Arnold Nobel described (**Nobel**; **2013**).

In the developed flow region, flow velocity can be calculated using the following equation:

$$u_{s,r} = \sqrt{\frac{k_1}{2}} * u_0 * \frac{D_n}{s} * e^{k_2 * \frac{r^2}{s^2}} \tag{3.18}$$

where $u_{s,r}$ is the jet velocity at an axial distance "s" and a radial distance "r" (sometimes written as $u_j(s,r)$), u_0 is the initial jet velocity at the nozzle exit, D_n is the nozzle diameter, and k_1 and k_2 are empirical constants. Fischer determined an average value of 77.2 ± 2 for k_1, and an average value of 87.3 ± 5 for k_2 (**Fischer**; **1979**).

The momentum flux (I) can be determined once the jet velocity (u_j) is known. The momentum flux is important because the turbulent jet is driven by momentum. The momentum flux on all cross sections of the jet flow is conserved (**Rajaratnam**; **1976**):

$$I(s) = \rho_w * 2\pi \int_0^{\infty} u_j(s,r)^2 * r * dr = I_0 \tag{3.19}$$

where I_0 is the momentum flux at the nozzle exit and can be simplified using the flow rate at the nozzle exit (Q_0):

$$\begin{aligned} I_0 &= \rho_w * Q_0 * u_0 \\ Q_o &= c_d * \frac{1}{4} * \pi * D_n^2 * u_0 \end{aligned} \tag{3.20}$$

c_d is the nozzle discharge coefficient, the value of which depends on the product of the contraction coefficient (c_c) and the loss coefficient (c_v). These coefficients vary depending on the design of the nozzle. The three most common nozzle designs and their respective coefficients are as follows:

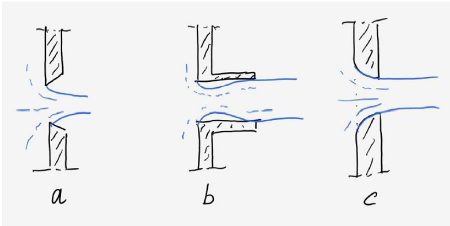

Figure 3.3: Most common nozzle design shapes (**Rhee**; **2018**).

Table 3.1: Nozzle Coefficient (**Rhee**; **2018**).

Nozzle	a	b	c
c_c [-]	0.62	1.0	1.0
c_v [-]	1.0	0.82	0.98
c_d [-]	0.62	0.82	0.98

According to **Albertson (1950)**, the values of k_1 and k_2 must be equal to 77 for the preservation of momentum. Therefore, for simplicity: $k_1 = k_2 = k = 77$.

3.2.1. IMPINGEMENT ZONE

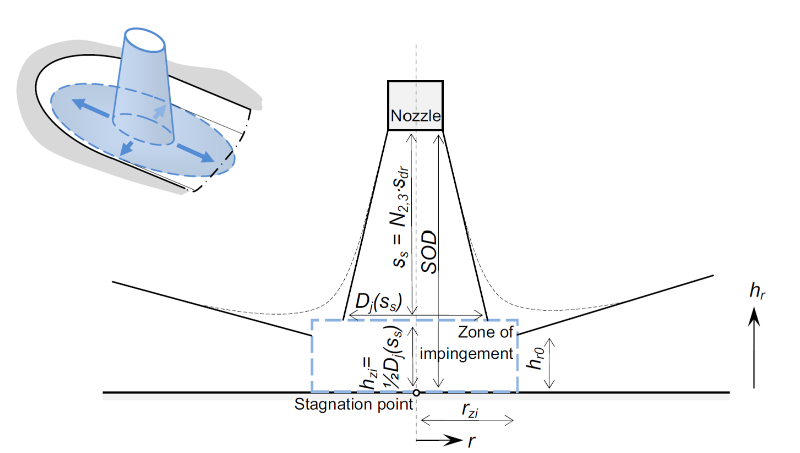

Figure 3.4: Vertical cross section of dispersing jet flow highlighting the zone of impingement (**Nobel**; **2013**).

The impingement zone is the specific area where the water jet impacts the soil surface and in where the jet flow is fully deflected (see Figure 3.4). The height of this zone is $\frac{1}{2} * D_j(s_s)$, where $D_j(s_s)$ is the fictitious jet diameter at the top of the zone (see Figure 3.4) and can be calculated using Equation 3.26 (**Nobel**; **2013**).

In the impingement zone, high pressure is exerted onto the surface by the water jet. This pressure can be significantly higher than the surrounding environment pressure. The kinetic energy of the water jet is converted into high pressure when it impacts the surface and this high pressure jet erodes the soil.

In **Nobel (2013)**, a constant stagnation pressure on the base of $\frac{1}{2}\rho_w u_u(s_s)^2$ is assumed, so a base diameter of $\sqrt{2}D_j(s_s)$ is needed to compensate the vertical momentum flux of the jet. Therefore, the diameter of the impingement zone is assumed to be $\sqrt{2}D_j(s_s)$.

The jet flow has a specific interaction with the surface when a water jet enters the impingement zone at an angle. The behavior of the jet in the impingement zone will depend on multiple factors such as the jetting angle, jet velocity, and soil properties. In general, the water jet will deflect away from its original path as it contacts the surface of the soil. The degree of deflection will depend on the jetting angle. The soil properties and the jetting velocity will help to determine if any of the soil will be displaced, or eroded. The impact of the water jet will generate a shearing force at the impingement zone and these forces can displace the soil.

3.3. NOZZLES

THREE nozzle diameters will be used for this study. Accordingly, we must determine three discharge coefficients (c_d). The following equation can be used to calculate an accurate discharge coefficient for each nozzle:

$$c_d = \frac{Q_0}{A_n * u_0} \tag{3.21}$$

where the jet flow (Q_0) is divided by nozzle surface (A_n) multiplied by the jet velocity (u_0). This leads to discharge coefficients of 0.99 for 12 mm, 17 mm, and 20 mm.

The jet is fully developed when the jet velocity of the flow field equals the initial jet velocity: $u_j(s,r) = u_0$. The distance at which fully developed flow is achieved can be calculated using the following equation (**Nobel**; **2013**):

$$s_{dr} = \sqrt{\frac{k_1}{2}} * D_n \approx 6.2 * D_n \tag{3.22}$$

Using Equation 3.5 and Equation 3.22, some parameters for this study can be established in the following Table 3.2:

Table 3.2: Calculated distances to the nozzle (s) and distances to the start of the fully developed flow region:

SOD	θ	s	D_n	s_{dr}
$5\ cm$	$25^o\&155^0$	$11.83\ cm$	$12\ mm$	$7.45\ cm$
$5\ cm$	$25^o\&155^0$	$11.83\ cm$	$17\ mm$	$10.55\ cm$
$5\ cm$	$25^o\&155^0$	$11.83\ cm$	$20\ mm$	$12.41\ cm$
$5\ cm$	$45^o\&135^0$	$7.07\ cm$	$12\ mm$	$7.45\ cm$
$5\ cm$	$45^o\&135^0$	$7.07\ cm$	$17\ mm$	$10.55\ cm$
$5\ cm$	$45^o\&135^0$	$7.07\ cm$	$20\ mm$	$12.41\ cm$
$5\ cm$	$65^o\&115^0$	$5.52\ cm$	$12\ mm$	$7.45\ cm$
$5\ cm$	$65^o\&115^0$	$5.52\ cm$	$17\ mm$	$10.55\ cm$
$5\ cm$	$65^o\&115^0$	$5.52\ cm$	$20\ mm$	$12.41\ cm$
$10\ cm$	$25^o\&155^0$	$23.66\ cm$	$12\ mm$	$7.45\ cm$
$10\ cm$	$25^o\&155^0$	$23.66\ cm$	$17\ mm$	$10.55\ cm$
$10\ cm$	$25^o\&155^0$	$23.66\ cm$	$20\ mm$	$12.41\ cm$
$10\ cm$	$45^o\&135^0$	$14.14\ cm$	$12\ mm$	$7.45\ cm$
$10\ cm$	$45^o\&135^0$	$14.14\ cm$	$17\ mm$	$10.55\ cm$
$10\ cm$	$45^o\&135^0$	$14.14\ cm$	$20\ mm$	$12.41\ cm$
$10\ cm$	$65^o\&115^0$	$11.03\ cm$	$12\ mm$	$7.45\ cm$
$10\ cm$	$65^o\&115^0$	$11.03\ cm$	$17\ mm$	$10.55\ cm$
$10\ cm$	$65^o\&115^0$	$11.03\ cm$	$20\ mm$	$12.41\ cm$

The equation for the uniform jet velocity in a fully developed circular free jet can be determined using the information gathered in the above Table 3.2.
When $s > s_{dr}$:

$$u_u(s) = \frac{1}{2} * \sqrt{\frac{k}{2}} * u_0 * \frac{D_n}{s} \tag{3.23}$$

Now, the fictitious jet diameter can be calculated:

$$D_j(s) = \sqrt{\frac{4}{\pi}\frac{Q(s)}{u_u(s)}} \tag{3.24}$$

Where the fictitious jet radius (r_u) is $\frac{1}{2}D_j(s)$.

When $s < s_{dr}$ the equation for the uniform jet velocity development in a fully developed circular free jet is:

$$u_u(s) = u_0 * \frac{D_n * \sqrt{\frac{k}{2}}}{s + D_n * \sqrt{\frac{k}{2}}} \tag{3.25}$$

and the fictitious jet radius is:

$$r_u(s) = \frac{1}{\sqrt{2 * k}} * s + \frac{1}{2} * D_n \tag{3.26}$$

The dynamic jet pressure at the point of impact on the clay can be determined using the uniform jet velocity:

$$p_j(s) = \frac{1}{2} * \rho_w * u_u(s) \tag{3.27}$$

For a stationary jet, the maximum depth at equilibrium, normalized by the stand-off distance, is a function of the Reynolds number ($\frac{u_0 * D_n}{\nu}$) and the non-dimensional parameter:

$$(\frac{D_n}{SOD})^2 * \frac{\rho_w * u_0^2}{\tau_c} \tag{3.28}$$

One can neglect the "turbulent flow" determined as the influence of a Reynolds number greater than $1 * 10^4$. During Arnold Nobel's jet tests, no Reynolds number lower than $5 * 10^5$ was found, and therefore, no effect of the Reynolds number was considered. Consequently, the non-dimensional parameter reduced to:

$$\frac{\rho_w * u_0^2}{\tau_c} \tag{3.29}$$

Assuming the critical shear stress (τ_c) is highly correlated to the undrained shear strength ($\tau_c \propto s_u$) for high jet pressure, this parameter can now be written as the "jet ratio" ($\frac{p_j}{s_u}$), since $p_j \propto \rho_w * u_0^2$ (**Nobel; 2013**).

Understanding the jet pressure and the undrained shear strength of the clay enables Nobel to determine the "jet ratio" ($\frac{p_j}{s_u}$). I can use this same ratio as a main factor to calculating the erosion depth.

3.3.1. PUMP PERFORMANCE CURVE

The pressure on the water pump was a significant design constraint. The "working point" (the intersection point) of the pump must be known to determine the flow-rate capability of each nozzle diameter. A "Pump and System" or "Performance" curve is used to determine the flow rate. There are three significant zones of a performance curve: "shutoff", "operating" or "working" point, and the "runout". The "working point" is the zone of great significance as it is the zone where the pump curve and the system curve intersect. The working point reveals the most efficient flow rate for each nozzle. The "runout" is the point on the pump curve farthest from the Y-axis. If the system operates near the runout, the motors will experience an overload current and the pump will decrease in reliability. The "shutoff" is the point on the pump curve closest to the Y-axis. If the system operates near the shutoff, the pump will have issues with maintaining the low flow rate. The performance curve of all three system curves can be seen in Figure 3.5 below.

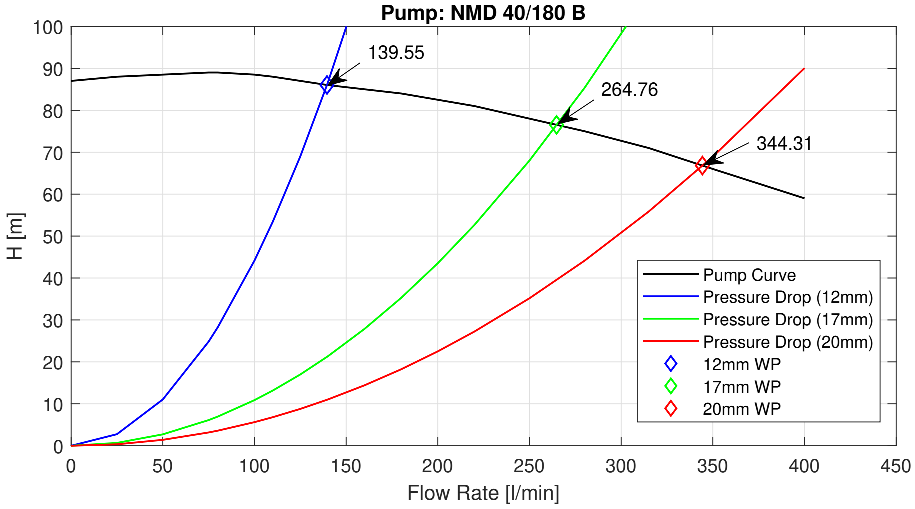

Figure 3.5: Pump curve showing working point (WP) of each nozzle diameter.

The flow rates are labeled at each of the working points in Figure 3.5. These flow rates will be used during testing. The 17 mm nozzle will be utilized most frequently because the working point for this nozzle is not located near the "shutoff" or "runout" of the pump curve, meaning that the pump will be the most reliable in delivering a constant flow rate with this set up. The other set-ups (20 mm and 12 mm) will also be tested. However, both nozzle set-ups must be closely monitored to ensure that the flow rate is constant throughout the test.

3.3.2. NOZZLE DESIGN

As indicated, three nozzles were designed for this study: 12 mm, 17 mm, and 20 mm nozzles. Three nozzles enable me to observe how the diameter of an inclined jet will affect the erosion of clay. The 17 mm nozzle will be tested at the six jetting angles discussed in Section 1.3 (25^o, 45^o, 65^o, 115^o, 135^o, and 155^o) to see the effect the jetting angle has on the erosion of clay.

Another design hurdle was that the half nozzles had to connect to the 38 mm diameter hose for the pump while also allowing the nozzles to lie flush with the side of the flume. It was necessary to angle the hose nozzle connection away from the wall-side of the nozzle to meet this design constraint. I chose a 22^o angle to keep the nozzle as straight as possible (see Figure 3.6). The different nozzle designs for the angles used can be seen in Figure 3.7, Figure 3.8, Figure 3.9, Figure 3.10, Figure 3.11, and Figure 3.12.

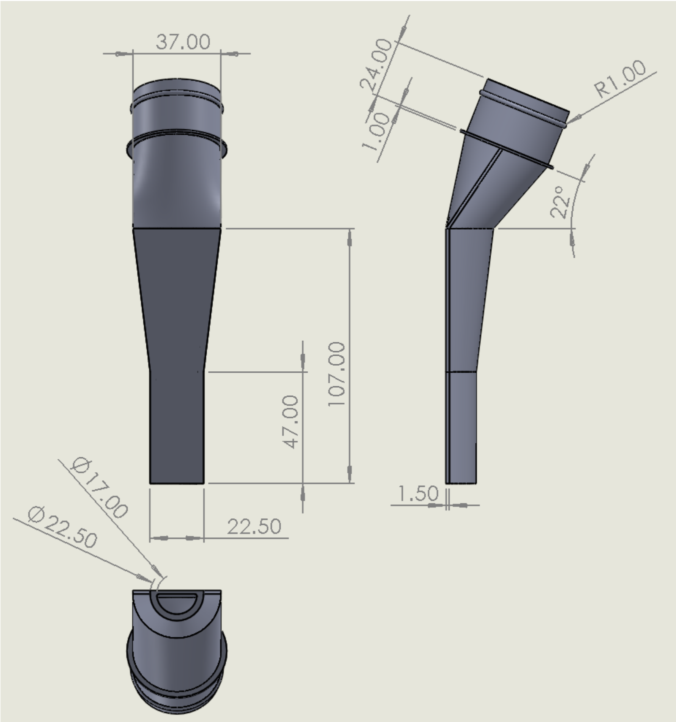

Figure 3.6: The SoildWorks design drawings for the 17 mm nozzle at 90^o with dimensions in mm.

The image on the right in Figure 3.6, illustrates the half nozzle design which permits the flat side of the nozzle to be placed against the flume glass thereby angling the hose connection away from the glass. The 22^o angle ensures that the hose will not contact the glass, thus allowing the nozzle to remain flush with the glass throughout the experiment. The hose connection portion of the nozzle has a bottom "lip". The lip prevents the nozzle from sliding too far into the hose during nozzle installation. The lip also ensures that each of the three nozzles are installed into the hose at uniform depth. A metal hose clamp will be placed on the outside of the hose between the bottom lip and top of the nozzle. This placement will secure the nozzle during testing.

The SOLIDWORKS design drawings for the 17 mm, 12 mm, and 20 mm nozzles can be seen in the following figures: Figure 3.7, Figure 3.8, Figure 3.9, Figure 3.10, Figure 3.11, and Figure 3.12.

3

These nozzles were 3D printed by the walk-in workshop at TU Delft using a "Form 3" resin printer.

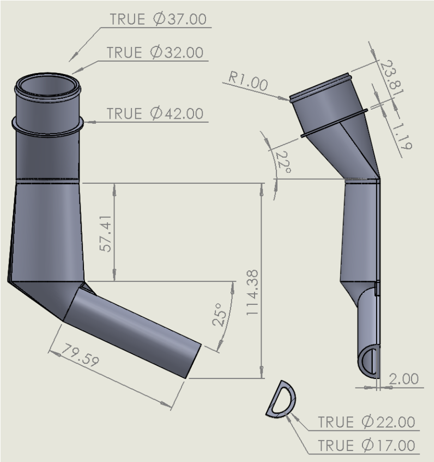

Figure 3.7: The SoildWorks design drawings for the 17 mm nozzle at angles $25^o/155^o$ with dimensions in mm.

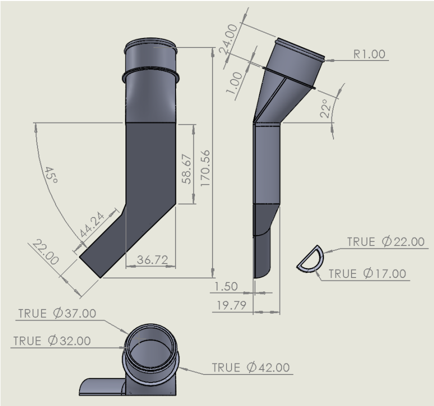

Figure 3.8: The SoildWorks design drawings for the 17 mm nozzle at angles $45^o/135^o$ with dimensions in mm.

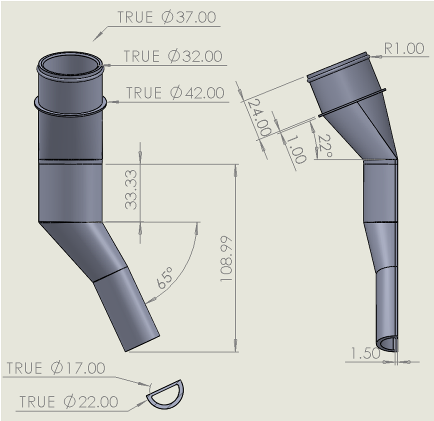

Figure 3.9: The SoildWorks design drawings for the 17 mm nozzle at angles $65^o/115^o$ with dimensions in mm.

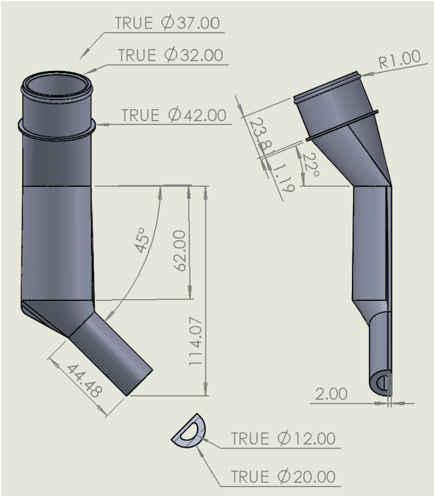

Figure 3.10: The SoildWorks design drawings for the 12 mm nozzle at angles $45^o/135^o$ with dimensions in mm.

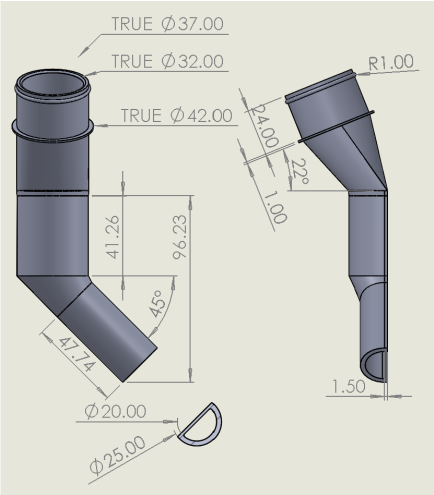

Figure 3.11: The SoildWorks design drawings for the 20 mm nozzle at angles $45^o/135^o$ with dimensions in mm.

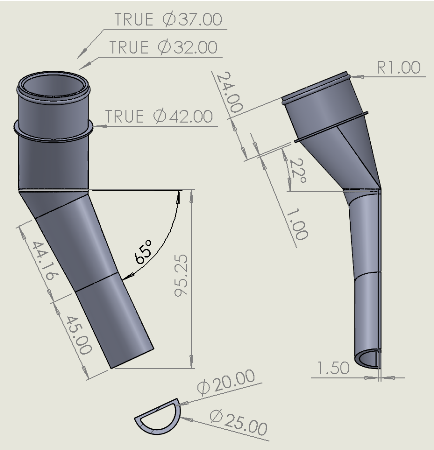

Figure 3.12: The SoildWorks design drawings for the 20 mm nozzle at angles $65^o/115^o$ with dimensions in mm.

3.4. EROSION

According to **Wang (2021)**, the soil failure process of cohesive soil is classified as "mass erosion" (or "bulk erosion") and can be very complex. The soil fails undrained and lumps of soil are torn from the bed by hydrodynamic stresses when a jet traverses the soil bed.

Machin and Allan (2011), emphasize that the erosion of sediment is significantly influenced by the exposure time and therefore the traverse velocity of the water jet. Other factors that Machin and Allan determined to be important were the permeability and the plasticity of the soil. In their experiments, Machin and Allan considered the cavity formation from a jet traverse velocity higher than $0.1-0.5\ m/s$ to be negligible (see Figure 3.13.

3

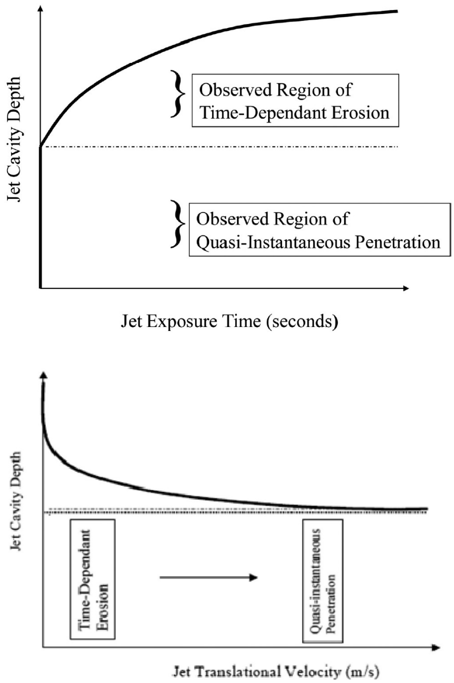

Figure 3.13: The observed cavity formation of **Machin and Allan (2011)**

Wang (2021) also models how the traverse velocity, v_t, has a significant impact on the erosion of soil. However, neither **Machin and Allan (2011)** nor **Wang (2021)** provide an equation using traverse velocity to determine the erosion depth. Instead, they provide figures demonstrating the relationship between the two (see Figure 3.13 and Figure 3.14).

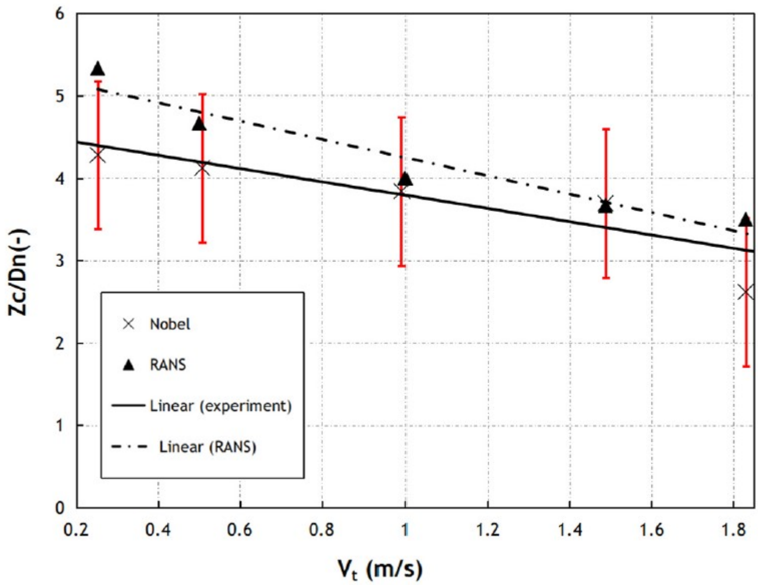

Figure 3.14: The dimensionless soil cavity depth at different jet traverse velocity when jet ratio $\frac{p_j}{s_u}$ = 19.5 at a SOD of 20 mm. (**Wang**; **2021**).

Bulk erosion is much harder to predict compared to "floc" and "surface" erosion that corresponds to milder flow conditions (**Wang**; **2021**). However, **Nobel (2013)** conducted several sets of experiments on the erosion process of clay due to a vertical water jet. Nobel's study can be used to estimate the erosion process of clay due to an inclined water jet. The estimates shown in Table 3.3 and Table 3.4 are possible using the equations described in **Nobel**; **2013**, and adjusting the inputs to account for the water jet being at an incline.

Using the information gathered from the Performance curve (Figure 3.5) and the nozzle design (Section 3.3.2), the jet ratio and the jet radius can be determined and used to calculate the expected width and depth of the cavity eroded by the water jet. The equations for the cavity width (W_c) and depth (Z_c) can been seen below (**Nobel**; **2013**):

$$W_c = D_n * (1 + \frac{s}{s_{dr}}) \tag{3.30}$$

Table 3.3: Cavity width comparison at a 45^o jetting angle and a *SOD* of 5 *cm*

D_n	s	s_{dr}	W_c
12 *mm*	7.07 *cm*	7.45 *cm*	2.34 *cm*
17 *mm*	7.07 *cm*	10.55 *cm*	2.84 *cm*
20 *mm*	7.07 *cm*	12.41 *cm*	3.14 *cm*

From the data in Table 3.3, it can be seen that as the nozzle diameters increase, so does the cavity width, which was to be expected.

$$\frac{Z_c}{D_n} \propto \frac{p_j}{su_p} \tag{3.31}$$

Table 3.4: Cavity depth comparison at a 45^o jetting angle and a *SOD* of 5 *cm*

D_n	$\frac{p_j}{su}$	Z_c
12 *mm*	8.81	5.29 *cm*
17 *mm*	10.67	9.07 *cm*
20 *mm*	10.60	10.60 *cm*

The values I calculated in Table 3.3 and Table 3.4 using Equation 3.30 and Equation 3.31 are used as an estimation of expectations during the experiment and will be used during the experiments to determine if the current equation is accurate at predicting the data being collected. The equations and values will be adjusted as needed after the results of the experiment are analyzed in Section 5.4. An updated equation for erosion depth will be derived and explained in Section 7.1.2

3.5. SUMMARY

THE foregoing research on water jets establishes a substructure for the experimental study, emphasizing critical factors such as traverse velocity, nozzle design, and pump performance. Chapter 5, Chapter 6, and Chapter 7 will aim to refine models, thereby contributing to a comprehensive understanding of cohesive soil erosion by water jets.

Water jets play a significant role in cohesive soil erosion, particularly in dredging and deep-sea mining. This chapter explores key principles, drawing insights from Nobel's experiments, and highlights crucial factors such as stagnation pressure, jetting angles, and impingement zones. Nozzle design and pump performance are identified as essential considerations.

Section 3.4 on erosion complexity delves into prior studies by **Wang (2021)** and **Nobel (2013)**, focusing on traverse velocity and contributing to an understanding of erosion due to a vertical water jet. Wang's CDF modeling and Nobel's experiments with vertical water jets also provide a basis for predicting erosion depth.

Considering insights from the cited research, it is inferred that inclined water jets may exhibit reduced effectiveness in eroding cohesive soil. The literature provides estimations for the resulting cavity depth and width from such jets. Armed with this knowledge, Section 7.1.2 presents an updated equation for predicting erosion depth.

4

Failure Modes of Cohesive Soil

4.1. Introduction

Cohesive soil will erode "fail" differently depending on the type of jet causing the erosion. Both **Nobel (2013)** and **Wang (2021)** use four failure modes to classify the type of jet, or erosion. These four modes are:

- Penetrating jet.
- Deflecting jet.
- Dispersing jet flow.
- Hydro-fracturing.

Since **Wang (2021)** used the data from **Nobel (2013)** for his modelling, the figures from **Wang (2021)** provide clear examples of the penetrating jet and deflecting jet failure modes while **Nobel (2013)** provides a detail definition of each failure mode, other than Hydro-fracturing. **Wang (2021)** defined hydro-fracturing briefly, however Wang did not focus his study on it. Wang states that hydro-fracturing occurs when $v_t < 0.15\, m/s$. He also adds that the soil cavity dimensions are irregular and the soil fails at its weakest point during hydro-fracturing (**Wang**; **2021**). As for **Nobel (2013)**, Hydro-fracturing was not a part of his or this study.

Wang (2021) adopts the failure mode definitions of **Nobel (2013)** and summarizes them into four main points (see Section 4.2, Section 4.3, and Section 4.4).

4.2. PENETRATING JET

IN a penetrating jet failure mode, the entire jet must penetrate the soil before deflecting backwards after a certain jet distance. The deflection zone is the zone wherein the jet starts to deflect backwards. With a penetrating jet, a non-deflection zone is clearly visible in contrast to the deflection zone (see Figure 4.1). **Nobel (2013)** concluded that the penetrating jet failure mode occurs when the cavity depth becomes larger than about 2.5 times the jet diameter at the original soil surface ($Z_c > 2.5 * D_n$) (**Nobel**; **2013**). Nobel also notes that the cavity width of a penetrating jet is much smaller than that of a deflecting or dispersing jet and is about equal to the jet diameter (see Figure 4.6 **(a)** and **(e)**).

Wang (2021) definition summary:

4

- A penetrating jet happens when $\frac{p_j}{s_u} > 12$ and $v_t \leq u_{f,h}$, where $u_{f,h}$ is the soil horizontal propagation velocity.
- The soil cavity is narrow and deep, with a cavity width of 1 - 1.5 times the jet diameter.
- A soil wall texture with vertical nerves (non-deflection zone) and curving nerves (deflection zone).
- The dislodged soil is completely fluidized.

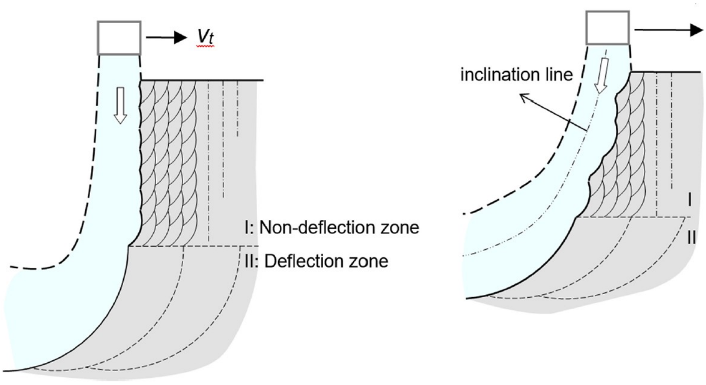

Figure 4.1: The two jet zones of a penetrating jet: Non-deflection (zone 1) and Deflection (zone 2) illustrated by **Wang (2021)**.

Figure 4.1 also shows that as the traverse velocity v_t, increases the non-deflection zone forms on an inclination line. This supports the claim that at a certain point ($v_t > u_{f,h}$) the jet is no longer classified as a penetrating jet.

4.3. DEFLECTING JET

DEFLECTING jets deflect backwards immediately after penetrating the soil. When this happens, the soil "fails" in large strips rather than small discrete soil elements (see Figure 4.2). **Nobel (2013)** concluded that this occurs when the cavity depth is smaller than about 2.5 times the jet diameter at the original soil surface ($Z_c \leq 2.5D_{j,ss}$) and the cavity width at the soil surface is larger than the jet diameter ($W_c > D_{j,ss}$) (see Figure 4.3).

Wang (2021) definition summary:

- A deflecting jet occurs when $7.3 < \frac{p_j}{s_u} < 12$ or $v_t > u_{f,h}$, where $u_{f,h}$ is the soil horizontal propagation velocity.
- The soil cavity is shallower compared with the penetrating jet and smaller than 2.5 times the nozzle diameter.
- A soil wall texture with curving nerves representing the deflection zone appears.
- There are limited dislodged soil lumps found after the experiments.

4

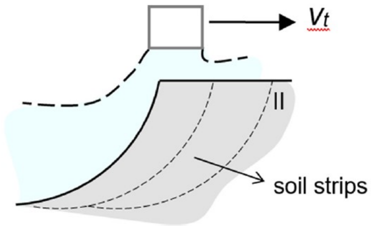

Figure 4.2: Illustration of the deflecting jet and its single deflection zone by **Wang (2021)**.

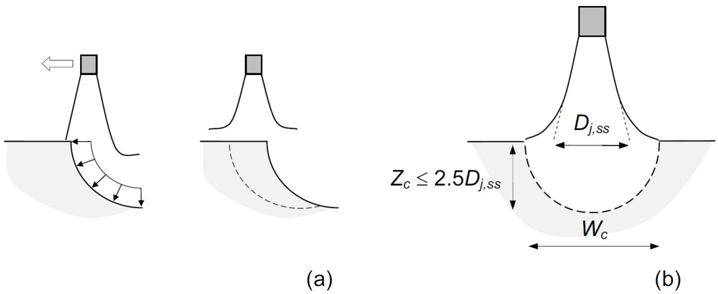

Figure 4.3: The deflecting jet defined by **Nobel (2013)**: **(a)** Failure mechanism (longitudinal cross section), **(b)** Deflecting jet definition (cross section, perpendicular to the traverse direction of the nozzle).

4.4. DISPERSING JET FLOW

A dispersing jet flow, will cause partial dispersion of the jet flow in the radial direction on the surface of the soil strip. When the stagnation pressure of the radial dispersing flow is high enough, the cavity can be widened by the flow. There are two failure mechanisms caused by a dispersing jet flow, "straight penetration" and "gradual penetration" (**Nobel**; **2013**).

Wang (2021) definition summary:

- Dispersing jet flow occurs when $5.4 < \frac{p_j}{s_u} < 7.3$ or $v_t >> u_{f,h}$.
- The depth of the cavity is shallow while the width of the cavity is greater, which can be equal to 5 times the nozzle diameter.
- The soil wall structure is irregular.
- The dislodged soil can be found after the experiments.

In "straight penetration", the jet penetrates directly to its final depth before the jet flow begins to disperse (see Figure 4.4). **Nobel (2013)** observed this during laboratory tests with small jet ratios ($\frac{p_j}{s_{u,p}}$). The dispersing jet flow can only widen the cavity when the required stagnation ratio for the radial soil failure is smaller than in the vertical direction, which is assumed to be equal to the bearing capacity factor, N_{bc} (**Nobel**; **2013**).

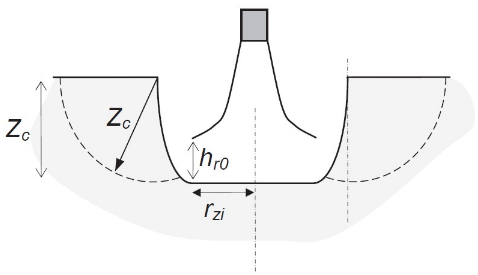

Figure 4.4: **Nobel (2013)** definition of a dispersing jet flow, straight penetrating to the maximum depth before dispersing. Where Z_c is the cavity depth, r_{zi} is the radial distance at the edge of the impingement zone, and h_{r0} is the radial jet flow height.

"Gradual penetration" occurs when the jet flow is continuously dispersing as the shearing process occurs. This widens the cavity gradually in multiple layers. "Gradual penetration" results in very wide and shallow cavities (see Figure 4.6 **(d)**) (**Nobel**; **2013**).

Wang (2021), created models of the penetrating jet and deflecting jet failure modes. The comparison between the modes is better visualized as a result. In Figure 4.5 it is easily seen that the penetrating jet reaches a maximum depth before starting to deflect, while the deflecting jet starts to deflect immediately upon contact with the soil.

I will adopt the definitions described in Section 4.2, Section 4.3, and Section 4.4 to classify failure modes of the clay due to an inclined water jet. Since **Nobel (2013)** worked with only 90^o nozzles, some adjustments may be required to properly define the failure modes caused by an inclined jet.

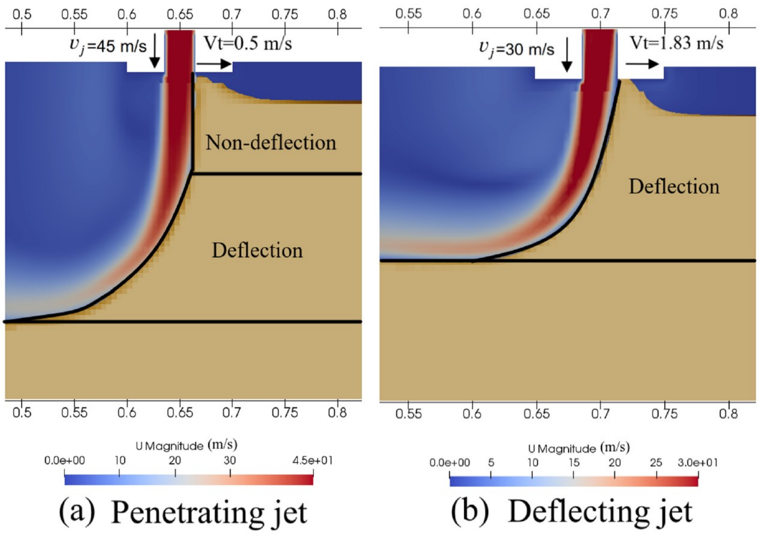

Figure 4.5: The fluid velocity and cavity shape of a penetrating jet **(a)** and a deflecting jet **(b)**. The soil is represented by the brown area and the the blue to red color scale represents the magnitude of the fluid velocity (**Wang; 2021**).

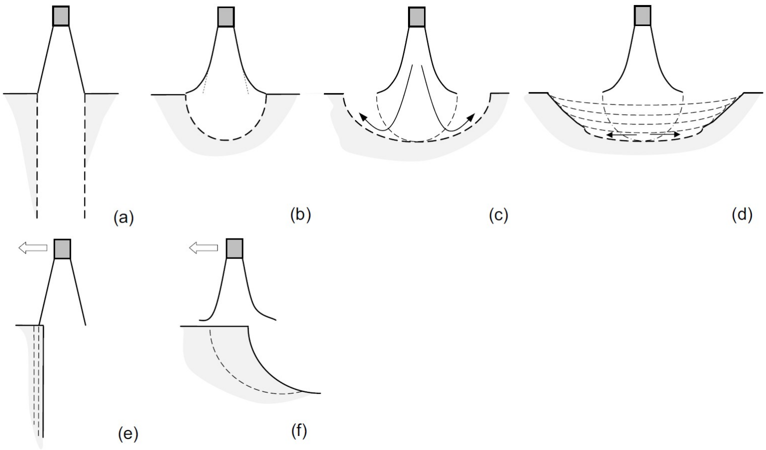

Figure 4.6: The failure modes defined by **Nobel (2013)**: **(a)** and **(e)** Penetrating jet, **(b)** and **(f)** Deflecting jet, **(c)** Dispersing jet flow, straight penetration, **(d)** Dispersing jet flow, gradual penetration (**a-d**: cross sections, perpendicular to the traverse direction of the nozzle, **e-f**: longitudinal cross sections) (**Nobel**; **2013**).

4.5. SUMMARY

I draw on the works of **Nobel (2013)** and **Wang (2021)** to explore the failure modes of cohesive soil under the impact of an inclined water jet. The identified failure modes include penetrating jet, deflecting jet, and dispersing jet flow. The penetrating jet involves complete soil penetration before backward deflection, characterized by a deep and narrow cavity. Deflecting jets deflect immediately after penetration, causing soil failure in large strips with a shallower cavity. Dispersing jet flow results in partial dispersion, with "straight" and "gradual" penetration modes causing widening cavities. **Wang (2021)** provides models and definitions, emphasizing factors such as jet velocity and soil cavity dimensions. Adjustments for inclined jets are suggested, adding valuable insights to the understanding of cohesive soil erosion.

The experimental phase must be executed to fully comprehend the erosion dynamics induced by a submerged inclined water jet and to address the research objectives outlined in Section 1.2. By comparing theoretical calculations with empirical results, the study aims to offer conclusive insights, as detailed in the final discussion in Section 8.1.

5

The Experiment

5.1. Introduction

The Experiment entails securing blocks of cohesive soil inside a flume along a transparent wall. A water jet set at various heights and angles will make several passes along the length of the flume wall. Elevation measurements are taken before and after each pass. The erosion depth is the difference between elevation measurements. Each test was recorded by video and photographs. Images of the set-up and the test rig model can be seen in Section 5.2. Images of the tests can be seen in Section 5.5.

The experiment intentionally resembles to Noble's precedent work. Notable distinctions include alterations in nozzle diameters, the soil sample composition, and the jetting angles. A comprehensive description of the experimental set-up is explained in Section 5.2, which expands upon the specific methodologies and apparatus employed to execute the testing.

5.2. EXPERIMENTAL SET-UP

I will conduct the experiment within a small flume provided by TU Delft. This endeavor will investigate 15 distinct combinations. Each combination is characterized by a unique interplay of nozzle diameter (12, 17, 20 mm), jetting angle (25^o, 45^o, 65^o, 90^o, 115^o, 135^o, and 155^o), stand-off distance ($SOD = 5$ and 10 cm), and jetting direction (right to left '+', left to right '-'). Detailed information regarding the properties of the clay, a pivotal element in these experiments, can be found in Chapter 2 of this study.

A high-speed camera will be used to collect visual data from the experiment and measurements of the cavity depth and width will be collected after each test. The data recorded during each pass will include the angle of the jet and the stand-off distance. I will video record each pass to examine the erosion of the sediment. A "Calpeda" water pump (**NMD 40/180-B**) will be used for testing. The pump is a close coupled centrifugal pump with a production sheet showing a discharge range of 125 - 400 L/min, which will be sufficient for testing.

5

A flow meter will assure that we are achieving the correct flow for the experiment. An electromagnetic flow meter (EMS) is a volumetric flow meter that works based on Faraday's Law of Electromagnetic Induction. This principle states that when a conductive medium passes through a magnetic field, a voltage is generated that is proportional to the velocity of the medium, the density of the magnetic field, and the length of the conductor. (**Bharadwaj**; **2019**)

A focal point of this experiment is the clay block that will be centrally positioned within the flume, with one side securely pressed against the glass surface. To mitigate any softening of the clay, careful measures will be implemented to ensure that the clay block remains submerged for the briefest possible duration, and not to exceed one hour. A high-speed camera will be calibrated to focus on the clay blocks, which will be positioned at a distance of approximately one meter from the flume. The water jet, equipped with a half nozzle, will be situated at one end of the flume, positioned as close as possible to the glass side of the flume. A detailed account of the step-by-step set-up procedure is seen in the images below.

A notable challenge emerged during the design phase. The concern centered on the necessity for the nozzles to maintain the ability to adjust positioning, in terms of both varying angles and heights, while ensuring firm contact with the glass surface of the flume. To overcome this challenge, a part assembly was designed employing the 3D CAD program "Solidworks". This component is fashioned to secure itself to the hose and be seamlessly integrated into the rail system, as illustrated in Figure 5.1. The hose attachment is engineered at an inclined angle, permitting a horizontal sliding motion to allow for the adjustment of the nozzles' height.

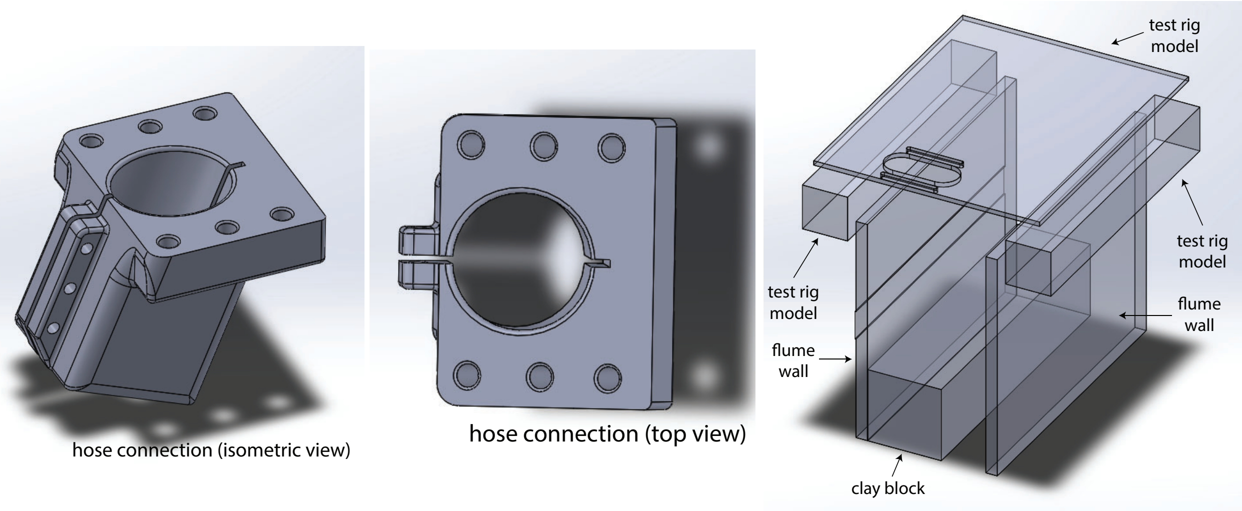

Figure 5.1: The SoildWorks part design (left and middle) used to secure the hose and nozzle to the test rig (right).

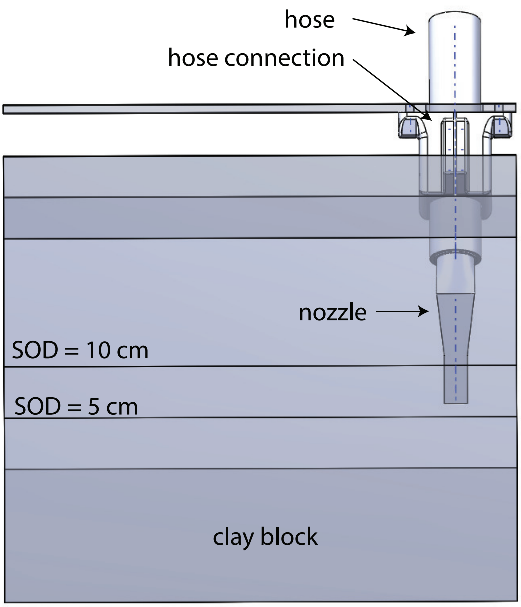

Figure 5.2: The SoildWorks design for connection of the hose to the rail system at 90^o.

The arrangement shown in Figure 5.2 is the control configuration in this experimental framework. This control set-up is integral to the study, serving as a reference point for comparison, as prior tests involving vertical nozzles have been extensively documented. The incorporation of this control facilitates a straightforward comparison between the performance of the "standard" vertical nozzles and the novel inclined nozzle configurations under investigation.

Figure 5.3: Overview of test set-up: This view allows one to see the work space I had available. The black cover around the work space was to minimize light glare on the cameras. The clay was back lit to increase the contrast and make the erosion process easier to see on camera.

Figure 5.4: Flume test set-up: These images depict how the test rig was set-up and the overall appearance of the flume with the test rig mounted to it. There are three views available: front (top), angled (middle), and side (bottom).

Figure 5.5: Pump test set-up: Hoses (yellow) were connected from the water tank (left) to the water pump (right) which was then routed from the water pump to the flow meter. The hose was then connected from flow meter to the nozzle and testing rig. This figure shows the blue cart used to hold the water pump (right, bottom) and the flow meter (right, top).

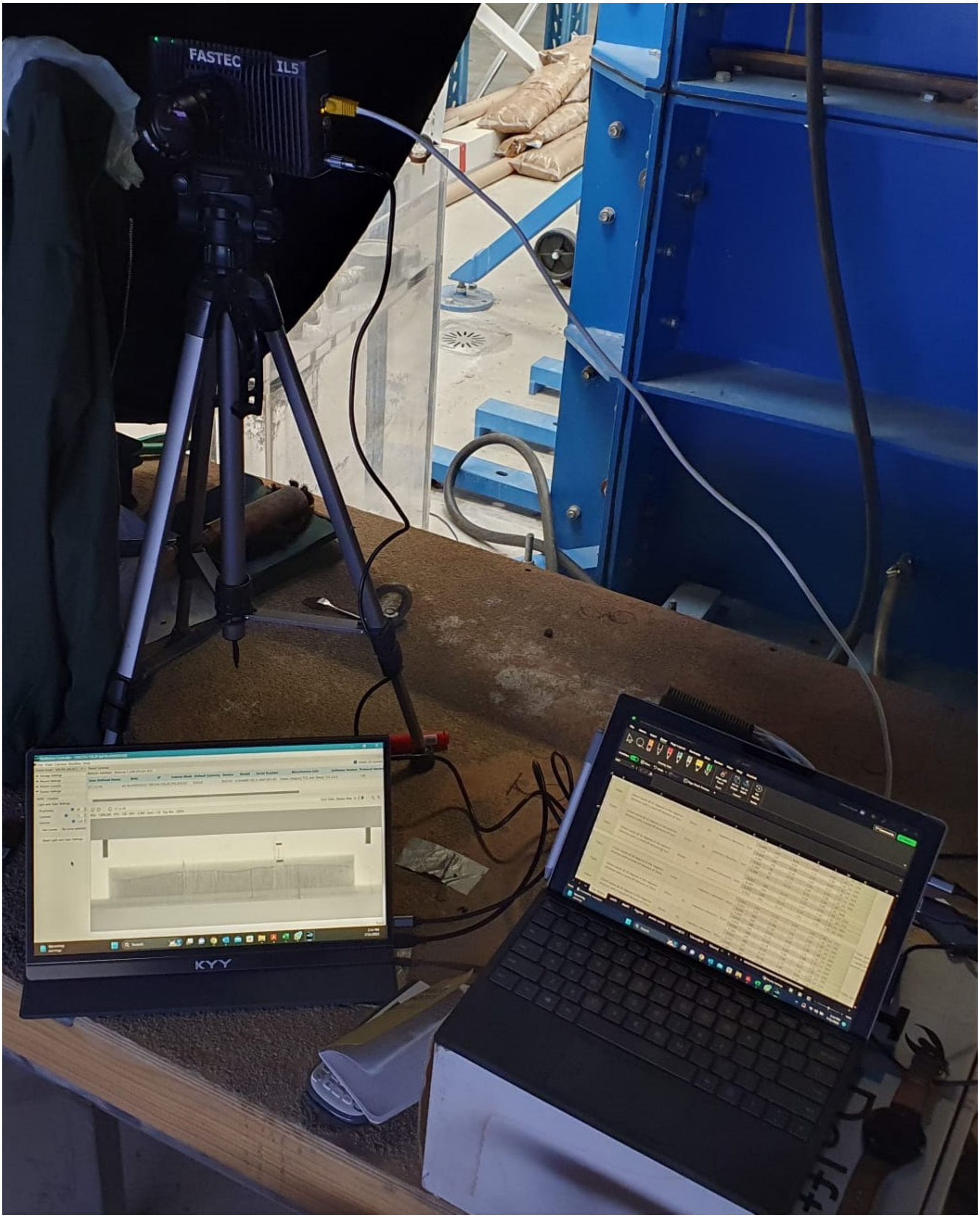

Figure 5.6: High-speed Camera test set-up: The high-speed camera was powered by it's own power cable and connected to my computer via an Ethernet cable. I then opened the cameras viewing an operating program ("FasMotion") on my second monitor.

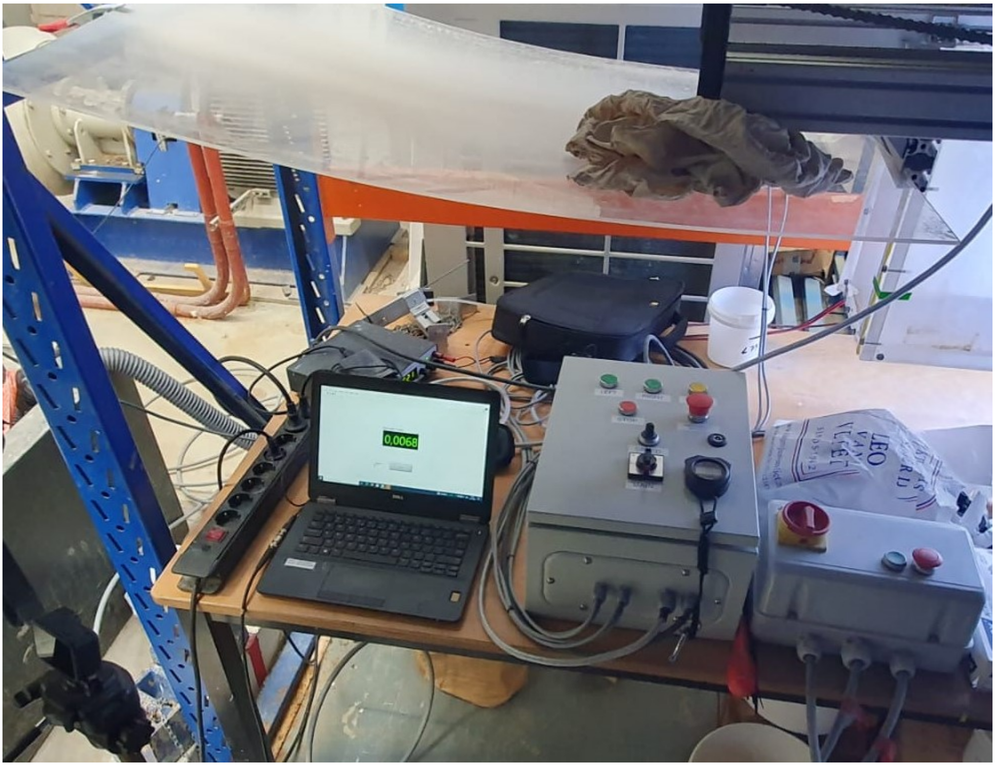

Figure 5.7: Electronics test set-up: The electronics for these experiments included a flow meter (computer on the left), the rail system controls (middle), and the pump controls (right). An acrylic cover was placed above the electronics to prevent and water from damaging the equipment.

Figure 5.7 depicts the electronics for operating the rail system and flow meter. The computer on the left of the set-up continuously measures the flow through the flow-meter. A camera was placed in front of the screen so that a recording of the flow could be made during each test. This recording was used to determine the flow during the test. To the right of the computer are the controls for the rail system. These controls included a dial for controlling the forward speed of the nozzle, which was calibrated every time the power switch was turned off and on. There were also two green "start" buttons, one to move the rig to the left and one to move the rig to the right. There was one red "stop" button. The stop button was not used during testing since there were sensors placed on the rail to ensure that the rig stopped at the same place each test. To the right of the rail controls were the water pump controls, which consisted of an "on" and "off" button for the pump.

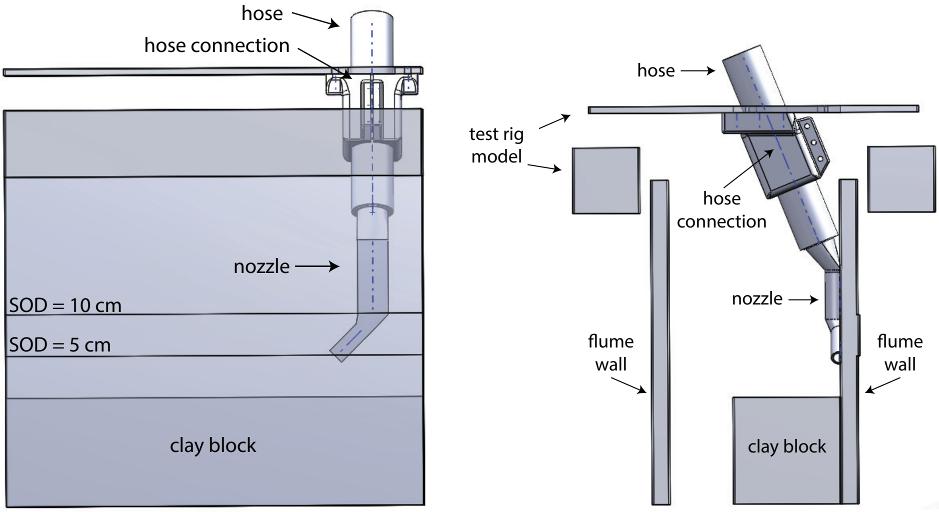

Figure 5.8: The SoildWorks design for connection of the hose to the rail system at 45^o. The image on the right illustrates the nozzle against the glass wall of the flume and located 5 or 10 cm above the clay block (bottom square) depending on the test that is being conducted.

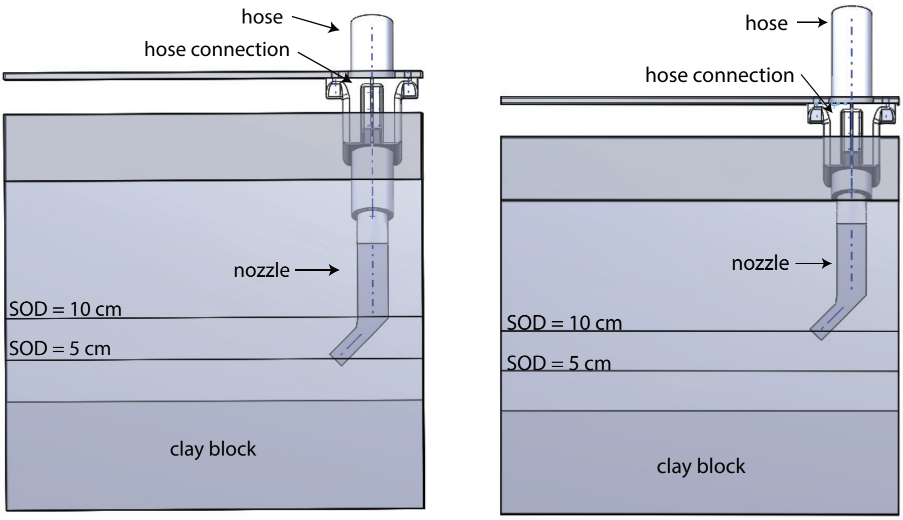

Figure 5.9: The SoildWorks design for connection of the hose to the rail system at 45^o. The image on the left illustrates the nozzle 5 cm above the clay block (bottom rectangle) while the image on the right illustrates the nozzle 10 cm above the clay block.

5.3. EXPERIMENT PROCEDURE

THE experiment consists of 27 steps. Each step was meticulously followed to ensure that the same test is performed on each "Test Condition" and to minimize potential for error.

Tests were conducted in all combinations of nozzle diameter to jetting angle and at two different stand-off distances. The minimum number of tests is one pass for each combination and direction, which was a total of 14 passes with the jet. I wanted to test each combination multiple times (a minimum of four times for each combination) to reduce the likelihood of error. Four passes in each combination would total 56 passes of the jet. (This number can be increased if we conclude that more data is necessary.)

The 27 steps are as follow:

1. Place two clay block in middle of the flume and secure them to the side of the flume by pressing them against the glass until they will no longer move/separate from the flume wall.

2. Measure and mark the starting height of the nozzle and clay to which the cameras will be focused on.

3. Confirm that the high-speed camera is positioned so that the clay block is in clear view.

4. Connect the desired nozzle diameter (12 mm, 17 mm, or 20 mm) to the water jet, confirm the correct angle is selected (25^o, 45^o, 65^o, 90^o, 115^o, 135^o, or 155^o), and set the correct stand-off distance (5 or 10 cm).

For the water jet moving from right to left (25^o, 45^o, 65^o, 90^o):

5. The water jet will start on the right side of the flume with the nozzle pointing towards the clay block at the correct angle and at the correct stand-off distance.

6. Mark ten points equally spaced along the distance of the two clay blocks and measure the starting height of the clay at each of these points using a laser ruler.

7. The flume will then be filled to about 25 cm from the bottom of the flume (or just until the water jet is completely submerged). This is to prevent overflowing the flume once the test begins

8. Mark the starting position of the nozzle.

9. Start the high-speed camera.

10. Start the flow meter camera.

11. Start the GoPro, overview, camera.

12. Start the water jet, wait for the jet to reach the proper flow rate and commence the test.
    (a) The jet will run at a forward velocity, from right to left, of ≈ 0.4 m/s for the majority of the test (a variation of forward velocities will be tested as a variable in later tests).
    (b) Given that the flume is three meters long and the water jet will only travel about one meter, the test will take less than seven seconds for each pass of the jet.
    (c) There is a sensor at the end of the flume to ensure a quick stop of the carriage.
13. Turn off the water jet.
14. Pause and save the videos from the three cameras (Flow meter, GoPro, and High-speed camera).
15. Drain the flume.
16. Photograph of the clay block (make sure to capture the cavity depth and width).
17. measure the end height of the clay at the ten points that were marked in step 6.
    (a) The difference between the starting heights and end heights will be used as the erosion depth achieved by the nozzles.
18. Remove the clay block from the flume.
19. Repeat steps 1 - 18 for all combinations (for the water jet moving from right to left).

<u>**For the water jet moving from left to right** (115^o, 135^o, 155^o)**:**</u>

20. Repeat steps 1 - 4.
21. The water jet will start on the left side of the flume with the nozzle pointing away from the clay blocks at the correct angle and at the correct stand-off distance.
22. Repeat steps 6 - 11.
23. Start the water jet, wait for the jet to reach the proper flow rate and commence the test.
    (a) The jet will run at a forward velocity, from left to right, of ≈ 0.4 m/s.
    (b) Given that the flume is three meters long and the water jet will only travel about one meter, the test will take less than seven seconds for each pass of the jet.
    (c) There is a sensor at the end of the flume to ensure a quick stop of the carriage.
24. Repeat steps 13 - 18.

25. Repeat steps 20 - 24 for all combinations (for the water jet moving from left to right).

26. Make sure all data is saved and take care of any adjustments or mistakes that may have occurred during the experiment.

27. Experiment is complete.

5.4. EXPERIMENT REVIEW

THE experiment as a whole produced expected data. There were a few setbacks at different stages of the experiment. The first major setback was the difficulty of securing the clay block to the side of the flume during testing. Wedges were placed to press the clay against the glass; however, the pressure had to be controlled to avoid the risk of breaking the flume. As testing progressed, I became increasingly successful at securing the clay to the glass. Another issue was that some of the 3D-printed nozzles were unable to withstand the pressure that the experiment tried to achieve. Re-making the nozzles out of a new material was not practicable due to time and budgetary constraints. I was compelled to decrease the flow rate through the nozzle, which in turn would decrease the erosion depth. The decreased erosion depth meant that it was also necessary to decrease the allowable error. A laser ruler was used to measure the erosion depth to achieve a more accurate measurement.

5

5.4.1. CHALLENGES

THERE were a few challenges that appeared during testing. The first of these was that the lab technicians where unable to create the nozzle connection point to the rail system due to the complex way the nozzles needed to move and be secured. This unforeseen challenge cost two weeks of time, as I had to design and test a few different connection pieces before settling on a final design (see Figure 5.1). This design allowed me to secure the nozzles at my desired height while staying flush with the wall of the flume (see Figure 5.8).

Another challenge was the failure of the flow-meter to reach the target flow rate. This was due to the water pump and the flow-meter having different maximum flow outputs. This challenge could have been prevented by using a different flow meter. Unfortunately, this issue arose too late in the process and did not allow time to acquire a new flow-meter. Therefore, I had to make due with the flow rate I was getting with the flow-meter I had available. Ultimately, this issue was not as serious as originally thought. The 3D printed nozzles were unable to withstand pressure greater than what I was producing anyway - leading to a third challenge.

The third challenge was the failure of some of the nozzles under the pressure produced using the maximum flow rate available from the flow-meter. The possibility of the nozzles breaking under pressure was known; however, there was no data about the maximum pressure the nozzles could withstand. This was the first time the lab had printed nozzles from resin. To overcome this challenge, the broken nozzles where reprinted with thicker walls and more "fillet" corners to strengthen the connection points.

The struggle to maintain complete connection between the clay and the flume glass was another challenge. The force of the water jet on the clay would tend to peel/separate the clay from the wall of the flume. The separation would render the tests inconclusive because the water jet would divert through the gap between the wall and the clay rather than erode the clay. To solve this problem, I trimmed the clay before placing it into the flume. I started with one section and placed the clay against the wall making sure to press hard from the bottom up to remove any trapped air between the wall and the clay. Next, I placed the previously trimmed sections of clay into the flume making sure there was a tight fit between the clay and the spacer in the flume. I made sure that the area of the clay to be tested was smooth and evenly leveled to the best of my ability before testing and before the starting measurements were taken. By so doing, I ensured that the clay would not move or separate from the wall of the flume (see Figure 5.10).

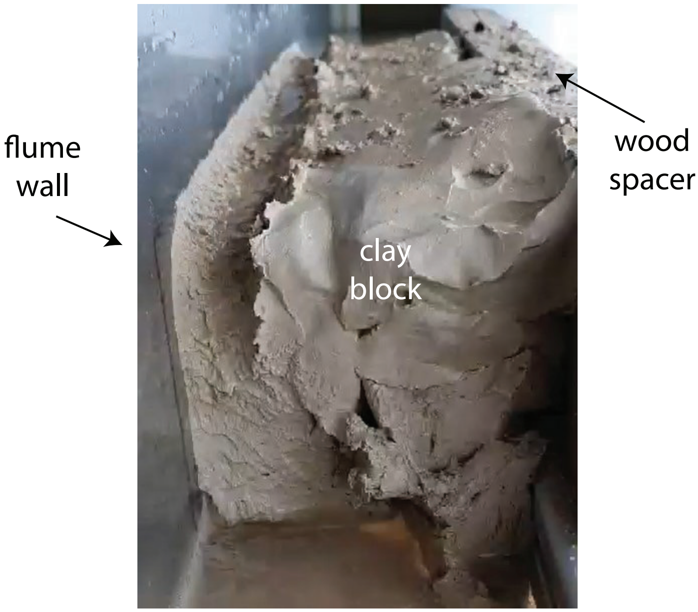

Figure 5.10: This figure demonstrates how the clay is secured between the wall of the flume and the wood spacer. The clay stays in place even after testing.

The last challenge I faced was that the slow-motion video I was using was not as helpful with measuring the erosion depth of the clay as I anticipated. The video was, however, helpful with visualizing the sediment plume. I switched to using a "laser" ruler for my erosion depth measurements since using the cameras to measure the depth was unreliable. This switch produced more accurate data and reduced the standard deviation of my data.

5.5. EROSION CLASSIFICATIONS

THIS section is dedicated to the examination of visual representations of the erosion process. To facilitate a coherent and standardized basis for comparison across different research papers, I have adopted the same three failure modes employed by both **Nobel (2013)** and **Wang (2021)** to categorize the type of jet behavior or erosion processes. These failure modes include:

- Penetrating jet.
- Deflecting jet.
- Dispersing jet flow.

For a more comprehensive understanding of these failure modes, a detailed description is provided in Chapter 4 of this thesis.

Throughout the course of these experiments, a "deflecting jet" failure mode was exhibited by all nozzle angles, aligning closely with the patterns described by **Nobel (2013)**. However, the 25^o, 45^o, and 65^o nozzles exhibit distinct behaviors, as evident in the video recordings of these tests. These nozzles display an atypical behavior where segments of the jet appear to deflect both forward and backward, as illustrated in Figure 5.11. This intriguing variation introduces a novel failure process that has not been explored in prior research, thereby enriching the understanding of jet behavior and erosion mechanisms.

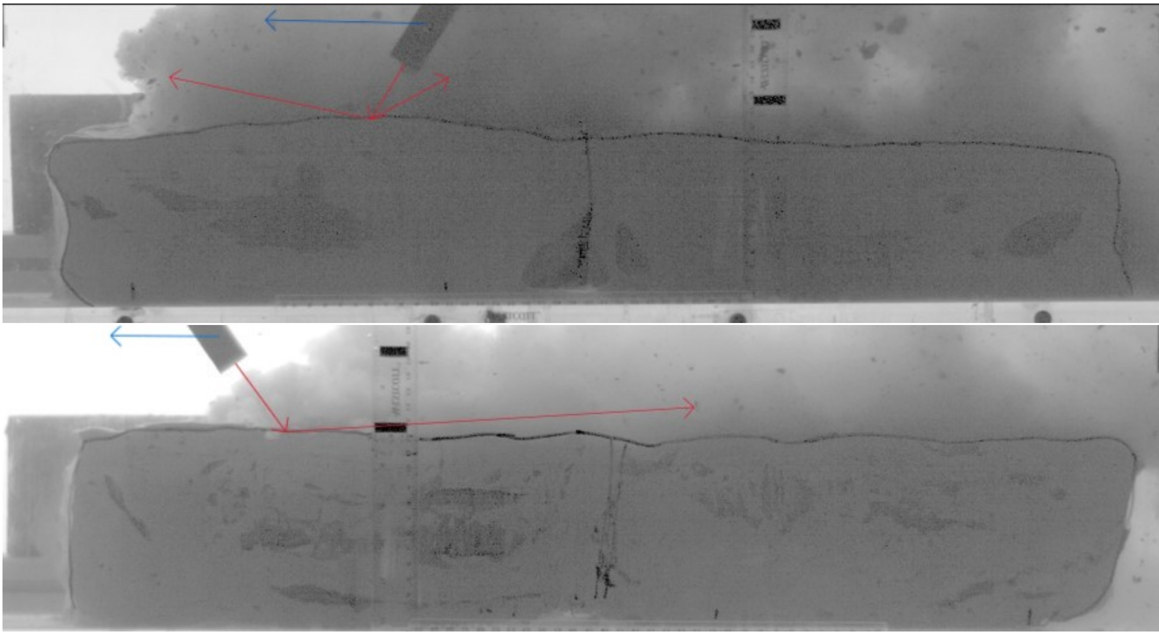

Figure 5.11: Comparison between jet deflection of the 45^o (top) and 135^o (bottom) nozzle. Where the blue arrow is the traverse direction of the nozzle and the red arrows are the approximate direction of the defected jet.

Below are top view images of the erosion for each test condition used during the experiment. One may notice that the closer the jetting angle is to 90 degrees the deeper the water jet penetrated into the clay. One might also notice how "clean" some of these "berms" (or edges of the erosion area) are compared to others, most notably: Figure 5.15 compared to Figure 5.18. these two angles are closely related and they produce similar erosion depths (see Figure 6.3) yet the "berm" in Figure 5.18 is much cleaner than the "berm" shown in Figure 5.15. I believe the jetting angle was the primary factor of influence on the condition of the "berm".

Figure 5.12: TC#01: 17 mm nozzle at a 90 degree jetting angle with a stand-off distance of 5 cm. The forward velocity was 0.422 m/s and there was a flow rate of 120 l/min producing a jet velocity of 11.90 m/s.

Figure 5.13: TC#02: 17 mm nozzle at a 25 degree jetting angle with a stand-off distance of 5 cm. The forward velocity was 0.419 m/s and there was a flow rate of 119.4 l/min producing a jet velocity of 7.78 m/s.

Figure 5.14: TC#03: 17 mm nozzle at a 45 degree jetting angle with a stand-off distance of 5 cm. The forward velocity was 0.429 m/s and there was a flow rate of 132 l/min producing a jet velocity of 11.55 m/s.

Figure 5.15: TC#04: 17 mm nozzle at a 65 degree jetting angle with a stand-off distance of 5 cm. The forward velocity was 0.414 m/s and there was a flow rate of 126 l/min producing a jet velocity of 12.09 m/s.

Figure 5.16: TC#05: 17 mm nozzle at a 155 degree jetting angle with a stand-off distance of 5 cm. The forward velocity was 0.396 m/s and there was a flow rate of 120 l/min producing a jet velocity of 11.90 m/s.

Figure 5.17: TC#06: 17 mm nozzle at a 135 degree jetting angle with a stand-off distance of 5 cm. The forward velocity was 0.400 m/s and there was a flow rate of 126 l/min producing a jet velocity of 11.02 m/s.

Figure 5.18: TC#07: 17 mm nozzle at a 115 degree jetting angle with a stand-off distance of 5 cm. The forward velocity was 0.402 m/s and there was a flow rate of 126 l/min producing a jet velocity of 12.09 m/s.

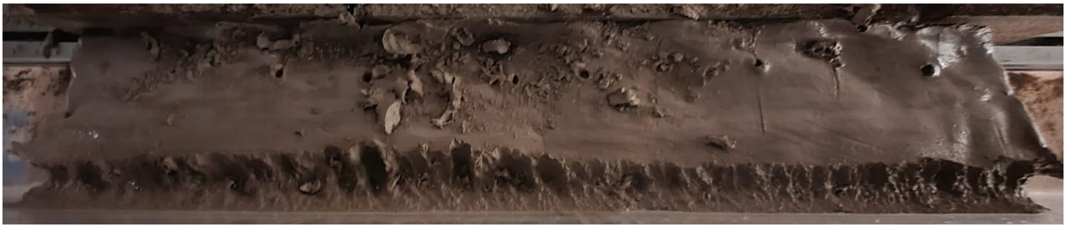

Figure 5.19: TC#08: 12 mm nozzle at a 45 degree jetting angle with a stand-off distance of 5 cm. The forward velocity was 0.428 m/s and there was a flow rate of 79 l/min producing a jet velocity of 11.93 m/s.

Figure 5.20: TC#09: 20 mm nozzle at a 45 degree jetting angle with a stand-off distance of 5 cm. The forward velocity was 0.411 m/s and there was a flow rate of 169 l/min producing a jet velocity of 11.31 m/s.

Figure 5.21: $TC\#10$: 12 mm nozzle at a 135 degree jetting angle with a stand-off distance of 5 cm. The forward velocity was 0.401 m/s and there was a flow rate of 81 l/min producing a jet velocity of 12.23 m/s.

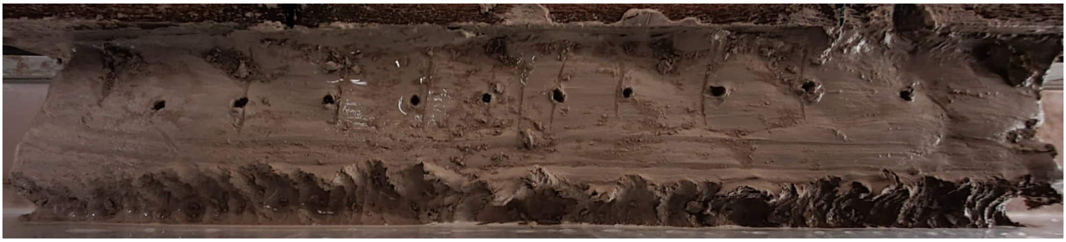

Figure 5.22: $TC\#11$: 20 mm nozzle at a 135 degree jetting angle with a stand-off distance of 5 cm. The forward velocity was 0.428 m/s and there was a flow rate of 177 l/min producing a jet velocity of 11.85 m/s.

Figure 5.23: $TC\#12$: 17 mm nozzle at a 90 degree jetting angle with a stand-off distance of 10 cm. The forward velocity was 0.431 m/s and there was a flow rate of 174 l/min producing a jet velocity of 17.25 m/s.

Figure 5.24: TC#13: 20 mm nozzle at a 45 degree jetting angle with a stand-off distance of 10 cm. The forward velocity was 0.448 m/s and there was a flow rate of 185 l/min producing a jet velocity of 12.38 m/s.

Figure 5.25: TC#14: 20 mm nozzle at a 65 degree jetting angle with a stand-off distance of 10 cm. The forward velocity was 0.412 m/s and there was a flow rate of 181 l/min producing a jet velocity of 10.09 m/s.

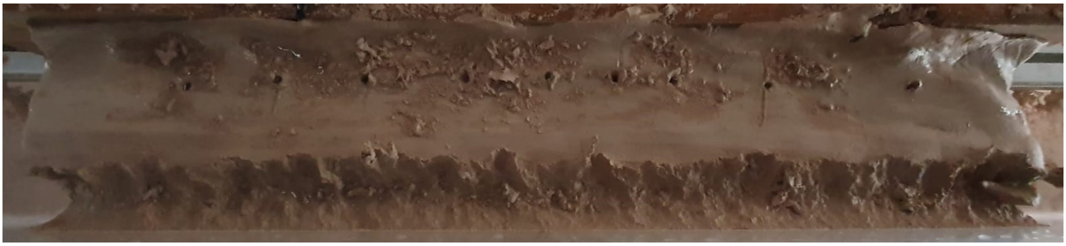

Figure 5.26: TC#15: 20 mm nozzle at a 65 degree jetting angle with a stand-off distance of 5 cm. The forward velocity was 0.443 m/s and there was a flow rate of 182 l/min producing a jet velocity of 10.12 m/s.

Using the definitions described in Section 4.3, one can see that the above photos depict a cohesive soil with a "deflecting jet failure mode". The soil cavity in each of the images is shallower than 2.5 times the nozzle diameter (the data provided in Chapter 6 will confirm). The soil wall texture also depicts "curving nerves" representing the deflection zone. After the experiment there were also limited dislodged soil lumps. These are all characteristics of a "deflecting jet failure mode" according to **Nobel (2013)** and **Wang (2021)**.

6

DATA ANALYSES

6.1. INTRODUCTION

THIS chapter is dedicated to the comprehensive analysis of experimental results. I will focus on the factors that impact the erosion process in cohesive soil. The outcomes presented herein aim to provide a thorough understanding of how variations in jetting angle, nozzle diameter, stand-off distance, and velocity impact the erosion behavior of cohesive soil specimens characterized by an undrained shear strength approximately equal to 25 kilopascals (kPa).

The analysis can be compartmentalized into four principal sections, each addressing a distinct experimental variable. In Section 6.2, titled "Jetting Angle," I delve into the effects of altering the angle at which the water jet impinges on the soil surface. In Section 6.3, "Nozzle Diameter," I explore how modifications in the diameter of the nozzle influence erosion dynamics. Section 6.4, "Stand-off Distance," is an in-depth exploration of the influence of varying stand-off distances on the erosion process. Lastly, in Section 6.5, "Forward Velocity," I unravel the consequences of manipulating the forward velocity of the jet on soil erosion. These four sections encapsulate the primary variables scrutinized in the experiment.

In addition to these core sections, I set aside a dedicated space for "Additional Results" in Section 6.6. This section will provide a platform for discussing supplementary findings and more general observations emerging from the experimental investigation that may offer valuable insights into the erosion behavior of cohesive soil.

6.2. JETTING ANGLE

As stated in Section 6.1, this section will focus on the analysis of the effects the jetting angle has on the erosion process of cohesive soil.

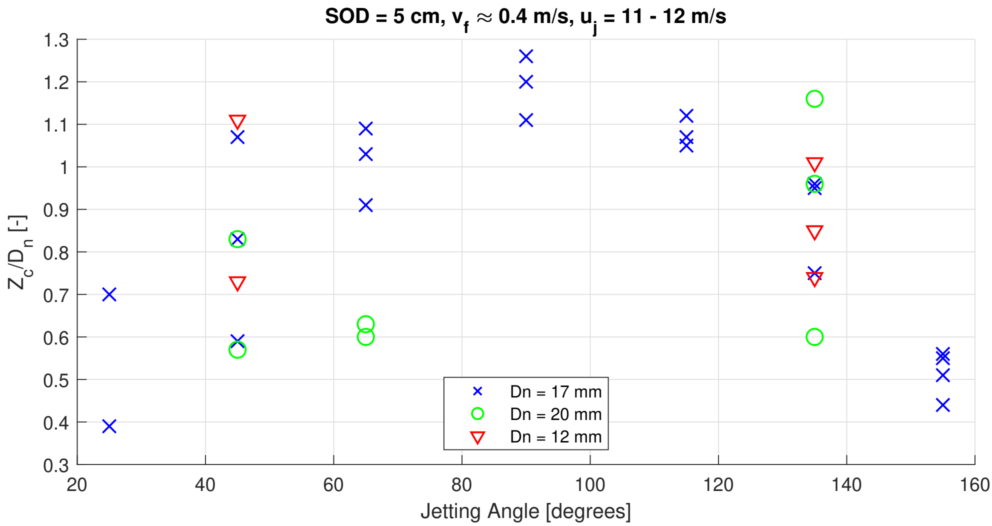

Figure 6.1: Effects of jetting angle on the dimensionless erosion depth (Z_c/D_n).

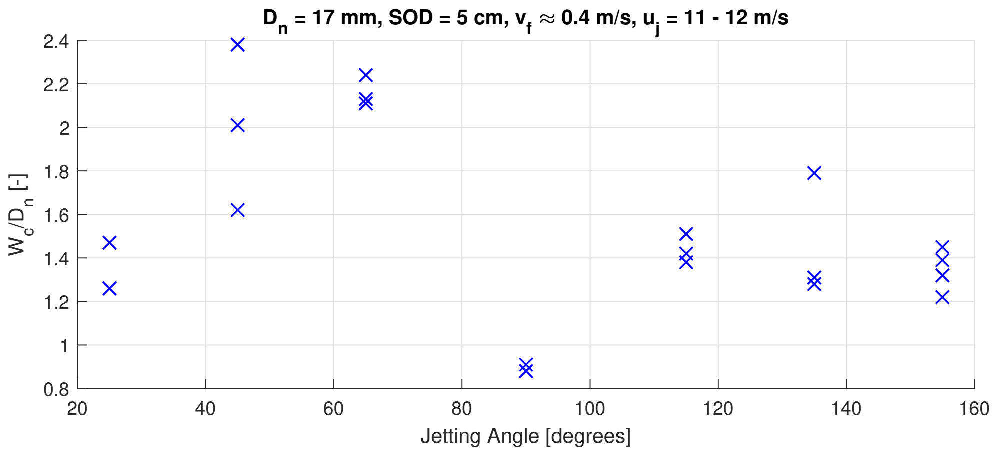

Figure 6.2: Effects of jetting angle on the dimensionless erosion width (W_c/D_n).

As expected, the erosion phenomena revealed a discernible trend concerning jetting angles. Specifically, the angles 25^o and 155^o exhibited relatively lower erosion characteristics compared to the more substantial erosion observed at steeper angles. In particular, nozzles oriented at angles of 65^o and 115^o demonstrated behavior closely resembling that of the 90^o angle, aligning with expectations because of their proximity to this benchmark angle. Finally, the erosion caused by the 45^o and 135^o nozzles appears to fit between the $25^o/155^o$ and the $65^o/115^o$ nozzles (see Figure 6.1).

It is noteworthy that an examination of the relationship between jetting angle and cavity width, as presented in Figure 6.2, reveals no discernible pattern or trend. This observation is consistent with the understanding that cavity width is primarily dictated by the jetting velocity and the undrained shear strength of the clay. In the context of this study, efforts were made to maintain these variables as constant as possible. Consequently, it was expected that the cavity width would exhibit little to no significant variation between jetting angles.

I adopted an approach to consolidate the data from the 17 mm nozzle as shown in Figure 6.1, leading to the construction of Figure 6.3 below, which is presented to enhance visualization of the data.

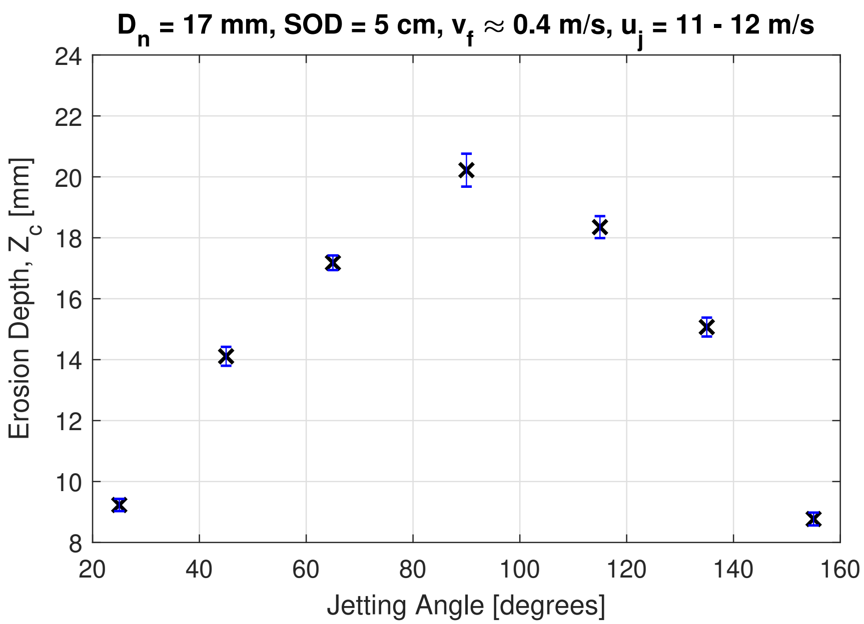

Figure 6.3: The average effects of jetting angle on the erosion depth, Z_c. The range markers for the data are indicated in blue and represent the standard deviations of my experimental data.

Figure 6.3 reveals a noticeable "bell curve" pattern that illustrates the efficacy of jetting angles on erosion, with the apex of this curve occurring with a nozzle positioned at a 90^o jetting angle. Prior research, such as the investigations conducted by **Wang (2021)**, **Wu (2018)**, and **Nobel (2013)**, were largely conjectural in their assessments of the impact of jetting angles on soil erosion. As one may notice, the erosion depths measured during the experiments are much smaller than the depths calculated in the previous equations

(Section 3.4). This demonstrates the need for an updated equation for erosion depth (that accounts for the jetting angle) to allow for a more accurate prediction of erosion depth. Leveraging the empirical data from these experiments affords us a more precise means to predict the consequences of varying jetting angles on the erosion of cohesive soil. Notably, in real-world scenarios, the orientation of nozzles relative to the irregular sea floor is rarely exactly 90^o due to the textural variations of the sea floor and the resultant "drag" experienced by suspended water jets. Thus, a comprehensive exploration into the optimization of jetting angles for water jets holds promise for enhancing the operational efficiency of dredge ships and, consequently, for reducing the overall operational costs incurred by dredging companies.

Additional observations pertain to the behavior of sediment plumes, particularly in relation to nozzle angles. Nozzles with angles exceeding 90^o, such as 115^o, 135^o, and 155^o, appear to confine the sediment plume predominantly behind the nozzle, yielding a more constrained and focused plume distribution (see Figure 6.4). In contrast, nozzles oriented at 90^o and smaller angles lead to a less predictable and more widely dispersed sediment plume (see Figure 6.5). This observation suggests there is practical potential for minimizing the sediment plume of a water jet in applications where such mitigation is desirable. Further exploration of this concept could yield valuable insights into sediment plume management strategies.

6

Figure 6.4: The sediment plume formed by a 12 mm water jet at 135^o (the jet is moving from right to left).

Figure 6.5: The sediment plume formed by a 17 mm water jet at 45^o (the jet is moving from right to left).

6.3. NOZZLE DIAMETER

THIS section will focus on the effects the nozzle diameter of an inclined water jet has on the erosion process of cohesive soil.

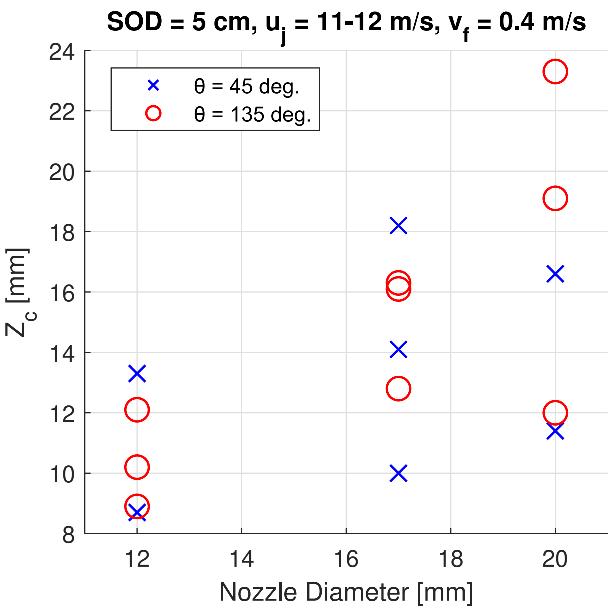

Figure 6.6: Effects of nozzle diameter on the erosion depth.

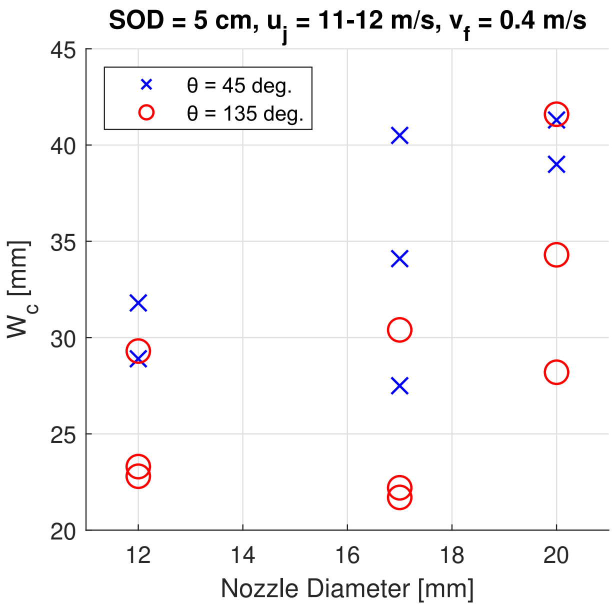

Figure 6.7: Effects of nozzle diameter on the erosion width.

6

Interestingly, the utilization of a 20 *mm* nozzle diameter resulted in erosion by a larger nozzle angle (135^o) that exceeded that of a smaller nozzle angle (45^o). The employment of a 12 *mm* nozzle diameter yielded the least erosion when considering points at both 45^o and 135^o. This outcome is expected since the entrainment of the surrounding water will affect the smaller nozzles area more than the larger nozzle area. There is more time for the entrainment of water to affect the water jet as the jetting distance increases. A 20 *mm* nozzle has a larger area and therefor there will be more “residual” or "core" jet after entrainment that allows for greater erosion.

A conspicuous trend emerges from the "depth graph" depicted in Figure 6.6. Erosion depth displays an incremental pattern with increasing nozzle diameter. A similar tendency is observable in the "width graph" albeit somewhat less conspicuous. The reason for this is that as the nozzle diameter expands, a greater volume water jet is brought into contact with the soil, resulting in a correspondingly increased erosion width.

6.4. STAND-OFF DISTANCE (SOD)

As stated in Section 6.1, this section will focus on the effects of the stand-off distance (SOD) of an inclined water jet on the erosion process of cohesive soil. I will compare distances of are 10 cm and 5 cm.

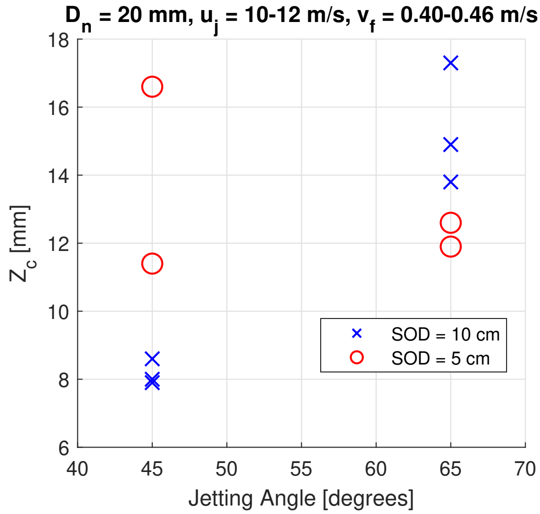

Figure 6.8: Effects of the stand-off distance (SOD) on the erosion depth, Z_c.

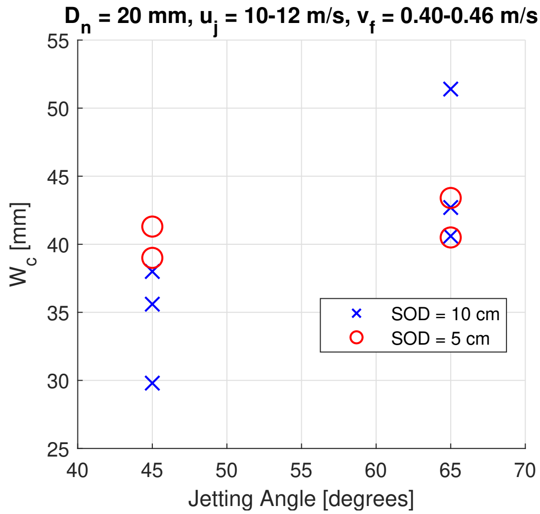

Figure 6.9: Effects of the stand-off distance (SOD) on the erosion width, W_c.

I observed that, for the water jets set at a 45^o angle, a Stand-Off Distance (SOD) of 10 cm results in a lesser degree of erosion compared to a SOD of 5 cm, aligning with initial expectations.

Intriguingly, in the case of water jets oriented at 65^o, a SOD of 10 cm yields a higher degree of erosion relative to a SOD of 5 cm (see Figure 6.8). The reasons for this divergence from expected behavior for the 65^o jetting angle may be related to entrainment. 65^o is a steeper angle than 45^o and therefore the jetting distance is longer for the nozzle at 45^o (see Figure 6.10 below). With a longer jetting distance, there is more time for entrainment to "reduce" the effective water jet leaving a smaller "core" area of the water jet that erodes the soil. This is apparent looking at data for the 45^o and 65^o nozzles at a SOD of 10 cm in Figure 6.8. One may wonder why this does not appear to be the case for a SOD of 5 cm. My theory on this phenomenon is that at 5 cm the difference in jetting distance between the two angles is not significant enough to noticeably affect the erosion depth and this is why Figure 6.8 displays similar erosion depths for both the 45^o and 65^o nozzle at a SOD of 5 cm. Further exploration would be essential to provide a better understanding of this occurrence. Presently, this can only be classified as speculation.

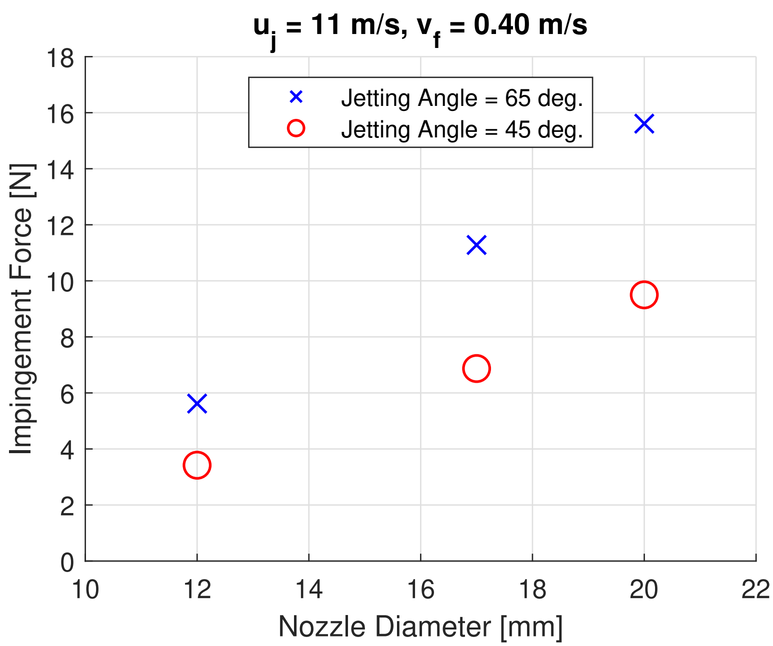

Figure 6.10: A demonstration of how the jetting angle effects the the vertical impingement force due to the increased jetting distance ($\theta = 65^o \rightarrow s = 0.055\ m$ and $\theta = 45^o \rightarrow s = 0.071\ m$.

6.5. FORWARD VELOCITY

THIS section will focus on the effect that the forward velocity of an inclined water jet has on the erosion process of cohesive soil. The range of velocities tested is 0.1 to 0.6 m/s, with the exact velocities tested marked with an "**x**" in Figure 6.11 and Figure 6.12.

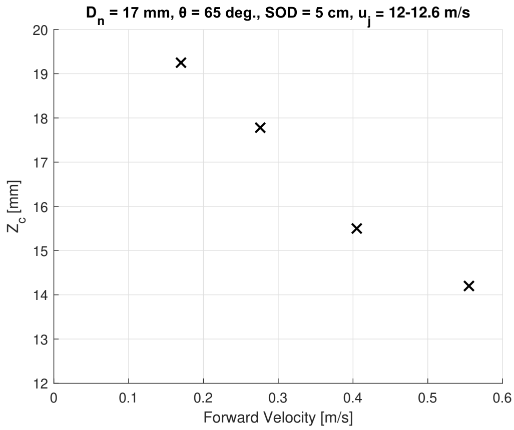

Figure 6.11: The effect the forward velocity, v_f $[m/s]$ of the nozzle has on the erosion depth, Z_c $[mm]$.

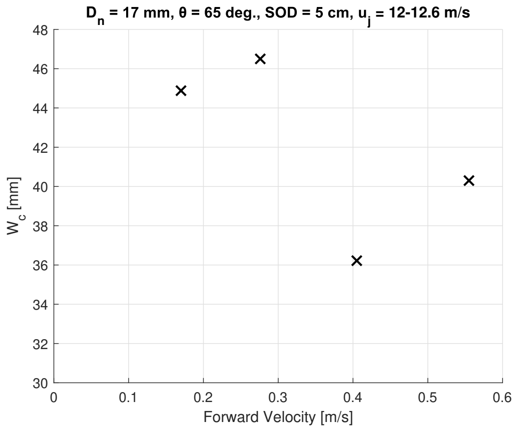

Figure 6.12: The effect the forward velocity, v_f $[m/s]$ of the nozzle has on the erosion width, W_c $[mm]$.

Figure 6.11 serves as a visual representation of the discernible influence of forward velocity on the depth of erosion in cohesive soil. It is observed that as the forward velocity of the water jet decreases, a prolonged interaction between the jet and the soil is afforded, permitting enhanced soil penetration and clay erosion. In contrast, there is a reduction in erosion depth with escalating forward velocities.

6.6. ADDITIONAL RESULTS

THE data analyzed in this section consists of more general information about the erosion process of cohesive soil. This data is not specific to one of the key study points discussed in Section 6.1. The findings presented in this section are additional observations that help to better understand the erosion process of cohesive soil.

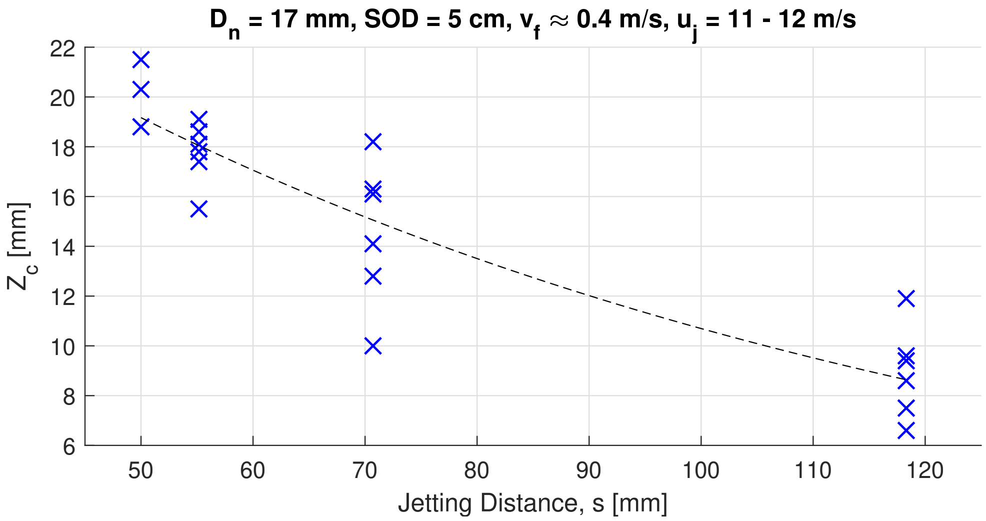

Figure 6.13: The erosion depth, Z_c $[mm]$ vs. the jetting distance, s $[mm]$.

Figure 6.13, is a visual representation of the impact of jetting distance, denoted as 's', on the erosion depth denoted as 'Z_c'. A trend is apparent, wherein an increase in the jetting distance leads to a decrease in erosion depth. This empirical relationship suggests the possibility of a specific jetting distance beyond which the erosion depth diminishes to the point of negligiblity. The correlation between jetting distance and erosion depth underscores the potential for optimizing the jetting distance as a critical parameter in the context of erosion processes where minimizing erosion depths may be a desirable outcome in certain practical applications.

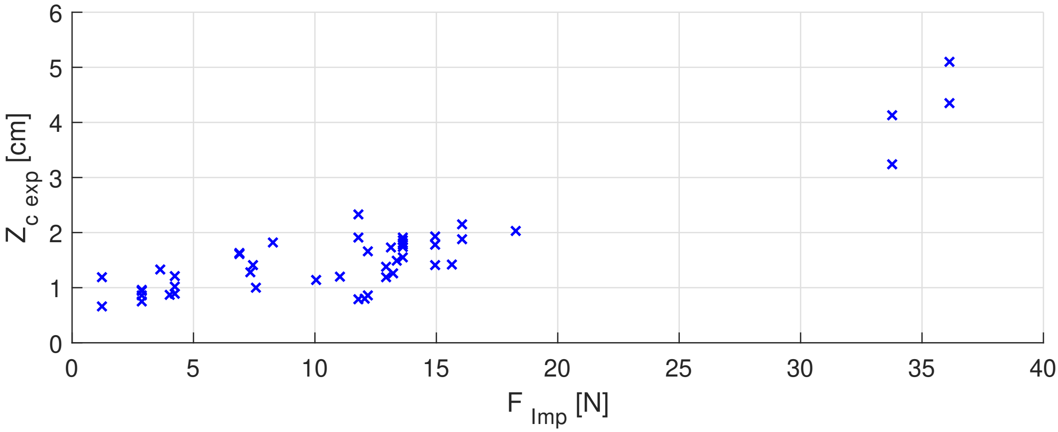

Figure 6.14: The relationship between the vertical Impingement Force, F_{Imp} $[N]$ and the measured erosion depth from the experiments, Z_{cexp} $[cm]$.

Figure 6.14 demonstrates the relationship between the vertical impingement force and the erosion depth measured during the experiments. As the vertical impingement force increases so does the erosion depth. This is to be expected since vertical impingement force is the force exerted on the soil surface at the point of impact. The more force exerted onto the soil surface the more likely erosion will occur.

6

The vertical impingement force, F_{Imp} is calculated by multiplying the nozzle area, A_n by the water density, ρ and the vertical component of the jet velocity, $u_{j,y}$:

$$F_{Imp} = A_n * \rho * u_{j,y}^2 \tag{6.1}$$

The vertical component of the jet velocity is used since this is the velocity that is contributing to the impingement force on the cohesive soil and is calculated as:

$$u_{j,y} = u_j * sin(\theta) \tag{6.2}$$

7
Research Objectives

7.1. Main results

Here, I detail the scientific and technical implications of this study. The primary findings of this thesis are presented in three separate sections, aiming to provide a straightforward conclusion for each research objective outlined in Section 1.2.

7.1.1. Visualize and Describe

Looking at the figures in Section 5.5, there appears to be a correlation between the jetting angle and the erosion classification. Using the classification criteria of **Nobel (2013)** and **Wang (2021)**, jetting with an inclined water jet appears to produce a "Deflecting Jet." However, the appearance of each cavity seemed to differ depending on whether the jetting angle was above or below 90^o. I believe that the jetting angle has a significant effect on the appearance of the cavity and the formation of the sediment plume during erosion. As seen in Figure 5.11, the larger the jetting angle the more controlled and predictable the sediment plume appears to be.

Based on the description by **Nobel (2013)** and **Wang (2021)** a "deflecting jet" failure mode was observed during testing. The cavity depths are less than 2.5 times the jet diameter at the original surface ($Z_c \leq 2.5D_n$). Additionally, the soil wall textures display curving nerves that indicates the deflection zone. I also found that a very limited number of soil lumps were dislodged during the experiments. These conditions are characteristic of a deflecting jet failure mode. Since these conditions were observed, and there was not sufficient evidence to suggest other failure modes (penetrating jet, dispersing jet flow, or hydro-fracturing), I can confidently classify the failure modes of the experiments conducted as a "deflecting jet" (see Figure 7.1 and Figure 7.2).

Figure 7.1: TC04-4: 17 mm nozzle angled at 65^o with a stand-off distance of 5 cm. The forward velocity was 0.414 m/s and there was a flow rate of 126 l/min.

Figure 7.2: TC07-4: 17 mm nozzle angled at 115^o with a stand-off distance of 5 cm. The forward velocity was 0.402 m/s and there was a flow rate of 126 l/min.

The videos taken during the experiments allow for views of sediment plume formation and reaction to the varying nozzle angles. I found that the main effect of the nozzle angle on the sediment plume is on containment and predictability of plume formation. For larger angles such as 115^o, 135^o, and 155^o (over 90^o) the sediment plume only forms behind the nozzle, whereas for smaller angles such as 25^o, 45^o, and 65^o, the sediment plume forms both in front and behind the nozzle (see Figure 7.3 and Figure 7.4). The formation in front of the nozzle causes a more unpredictable plume that disperses widely. If controlling or collecting the sediment plume is an objective, "larger" angles appear to be more effective than "smaller" angles at creating a predictable plume.

Figure 7.3: The sediment plume formed by a 17 mm water jet at 45^o (the jet is moving from right to left).

Figure 7.4: The sediment plume formed by a 12 mm water jet at 135^o (the jet is moving from right to left).

7.1.2. PREDICTING EROSION

Two assumptions must be made to proceed with calculating the erosion of the soil due to an inclined water jet. First, the erosion process is primarily influenced by the kinetic energy of the water jet. And second, the cohesive soil is modeled with undrained shear strength s_u.

Similar to **Liu (2023)**, using the "Buckingham π theorem", I have expressed variables by dimensionless equations to derive an equation for the erosion depth.

The Buckingham π theorem states that if there are **n** dimensional variables in a dimensionally homogeneous equation, described by **j** fundamental dimensions, they may be grouped in $k = n - j$ dimensionless groups. Each dimensionless group is called "**pi**" (or π). The relation among the dimensionless groups will be written in a method known as "method of repeating variables" and will look as such:

$$\pi_1 = f(\pi_2, \pi_3, \pi_4, ..., \pi_k) \tag{7.1}$$

The first step in the "Buckingham π theorem" is to list the contributing parameters in the problem. I identified the following parameters for when dealing with erosion depth:

$$Z_c, D_n, sin(\theta), P_d, s_u, s, v_f, u_j, \rho, g \tag{7.2}$$

where,

- Z_c: Erosion Depth (m)
- D_n: Nozzle diameter (m)
- θ: Jetting angle (degrees)
- P_d: Dynamic pressure $(Pa = \frac{kg}{s^2 m})$
- s_u: Undrained shear strength of the cohesive soil $(Pa = \frac{kg}{s^2 m})$
- s: Jetting distance (m)
- v_f: Forward velocity of the nozzle $(\frac{m}{s})$
- u_j: Jetting velocity $(\frac{m}{s})$
- ρ: Density of water $(\frac{kg}{m^3})$
- g: Gravity $(\frac{m}{s^2})$

I now count the number of **dimensional variables** and label this number as $n = 10$. Note that θ is the jetting angle measured in units of degrees, but does not have a "dimension". However, θ still needs a π group so it must be accounted for when determining "**n**."

The second step to the π theorem is to list the primary dimensions of each parameter.

Note: The dimensions of the parameters are different from the units of the parameters. For example the unit meters (m) is a "length" dimension and is labeled as (L), kilogram (kg) is a "mass" dimension and is labeled as (m), and seconds (s) is a "time" dimension and is labled as (t).

Table 7.1: Step two of the π theorem: List the primary dimensions of each parameter

Prameter	**Unit**	**Dimension**
Z_c	m	L
D_n	m	L
P_d	$\frac{kg}{s^2 m}$	$mt^{-2}L^{-1}$
s_u	$\frac{kg}{s^2 m}$	$mt^{-2}L^{-1}$
s	m	L
v_f	$\frac{m}{s}$	Lt^{-1}
u_j	$\frac{m}{s}$	Lt^{-1}
ρ	$\frac{kg}{m^3}$	mL^{-3}
g	$\frac{m}{s^2}$	Lt^{-2}
$sin(\theta)$	$degree$	$-$

I can observe that there are three primary dimensions involved in all parameters which are "m", "L", and "t". Therefore, the number of primary dimensions "**j**" is $j = 3$.

7

The third step of the π theorem is to calculate the number of dimensionless groups (k):

$$k = n - j = 10 - 3 = 7 \tag{7.3}$$

I can now re-write Equation 7.1:

$$\pi_1 = f(\pi_2, \pi_3, \pi_4, ..., \pi_7) \tag{7.4}$$

The forth step of the π theorem is to choose **j** repeating variables. $j = 3$, therefore, I choose 3 repeating variables that relate to mass (m), length (L), and time (t):

- mass: s_u $[mt^{-2}L^{-1}]$
- length: D_n $[L]$
- time: v_f $[Lt^{-1}]$

I can now move to step five of the π theorem, which is to construct the dimensionless groups. Each of the dimensionless π groups must contain these three repeating variables. To ensure the π groups are dimensionless I put "powers" on each of the repeating variables (a, b, c) and substitute the parameter dimensions identified in Table 7.1 to solve for the dimensionless groups:

$$\pi_1 = Z_c\, s_u^a\, D_n^b\, v_f^c = (L)\,(mt^{-2}L^{-1})^a\,(L)^b\,(Lt^{-1})^c$$
$$= (m^a)\,(LL^{-a}L^bL^c)\,(t^{-2a}t^{-c}) = m^a\,L^{1-a+b+c}\,t^{-2a-c} \Rightarrow$$
$$\mathbf{m}: 0 = a \rightarrow \mathbf{a = 0}$$
$$\mathbf{L}: 0 = 1 - a + b + c \rightarrow \mathbf{b = \text{-}1} \tag{7.5}$$
$$\mathbf{t}: 0 = -2a - c \rightarrow \mathbf{c = 0}$$
$$= Z_c\, s_u^0\, D_n^{-1}\, v_f^0 \; = \frac{Z_c}{D_n}$$

$$\pi_2 = P_d\, S_u^a\, D_n^b\, v_f^c = (mt^{-2}L^{-1})\,(mt^{-2}L^{-1})^a\,(L)^b\,(Lt^{-1})^c$$
$$= (mm^a)\,(L^{-1}L^{-a}L^bL^c)\,(t^{-2}t^{-2a}t^{-c}) = m^{1+a}\,L^{-1-a+b+c}\,t^{-2-2a-c} \Rightarrow$$
$$\mathbf{m}: 0 = 1 + a \rightarrow \mathbf{a = \text{-}1}$$
$$\mathbf{L}: 0 = -1 - a + b + c \rightarrow \mathbf{b = 0} \tag{7.6}$$
$$\mathbf{t}: 0 = -2 - 2a - c \rightarrow \mathbf{c = 0}$$
$$= P_d\, s_u^{-1}\, D_n^0\, v_f^0 \; = \frac{P_d}{su}$$

$$\pi_3 = s\, S_u^a\, D_n^b\, v_f^c = (L)\,(mt^{-2}L^{-1})^a\,(L)^b\,(Lt^{-1})^c$$
$$= (m^a)\,(LL^{-a}L^bL^c)\,(t^{-2a}t^{-c}) = m^a\,L^{1-a+b+c}\,t^{-2a-c} \Rightarrow$$
$$\mathbf{m}: 0 = a \rightarrow \mathbf{a = 0}$$
$$\mathbf{L}: 0 = 1 - a + b + c \rightarrow \mathbf{b = \text{-}1} \tag{7.7}$$
$$\mathbf{t}: 0 = -2a - c \rightarrow \mathbf{c = 0}$$
$$= s\, s_u^0\, D_n^{-1}\, v_f^0 \; = \frac{s}{Dn}$$

$$\pi_4 = u_j\, S_u^a\, D_n^b\, v_f^c = (Lt^{-1})\,(mt^{-2}L^{-1})^a\,(L)^b\,(Lt^{-1})^c$$
$$= (m^a)\,(LL^{-a}L^bL^c)\,(t^{-1}t^{-2a}t^{-c}) = m^a\,L^{1-a+b+c}\,t^{-1-2a-c} \Rightarrow$$

$$\begin{aligned} &\mathbf{m}: 0 = a \rightarrow \mathbf{a = 0} \\ &\mathbf{L}: 0 = 1 - a + b + c \rightarrow \mathbf{b = 0} \\ &\mathbf{t}: 0 = -1 - 2a - c \rightarrow \mathbf{c = \text{-}1} \end{aligned} \tag{7.8}$$

$$= u_j\, s_u^0\, D_n^0\, v_f^{-1} = \frac{u_j}{v_f}$$

$$\pi_5 = \rho\, S_u^a\, D_n^b\, v_f^c = (mL^{-3})\,(mt^{-2}L^{-1})^a\,(L)^b\,(Lt^{-1})^c$$
$$= (mm^a)\,(L^{-3}L^{-a}L^bL^c)\,(t^{-2a}t^{-c}) = m^1 + a\,L^{-3-a+b+c}\,t^{-2a-c} \Rightarrow$$

$$\begin{aligned} &\mathbf{m}: 0 = 1 + a \rightarrow \mathbf{a = \text{-}1} \\ &\mathbf{L}: 0 = -3 - a + b + c \rightarrow \mathbf{b = 0} \\ &\mathbf{t}: 0 = -2a - c \rightarrow \mathbf{c = 2} \end{aligned} \tag{7.9}$$

$$= \rho\, s_u^{-1}\, D_n^0\, v_f^2 = \frac{\rho v_f^2}{s_u}$$

$$\pi_6 = g\, S_u^a\, D_n^b\, v_f^c = (Lt^{-2})\,(mt^{-2}L^{-1})^a\,(L)^b\,(Lt^{-1})^c$$
$$= (m^a)\,(LL^{-a}L^bL^c)\,(t^{-2}t^{-2a}t^{-c}) = m^a\,L^{1-a+b+c}\,t^{-2-2a-c} \Rightarrow$$

$$\begin{aligned} &\mathbf{m}: 0 = a \rightarrow \mathbf{a = 0} \\ &\mathbf{L}: 0 = 1 - a + b + c \rightarrow \mathbf{b = 1} \\ &\mathbf{t}: 0 = -2 - 2a - c \rightarrow \mathbf{c = \text{-}2} \end{aligned} \tag{7.10}$$

$$= g\, s_u^0\, D_n^1\, v_f^-2 = \frac{gD_n}{v_f^2}$$

7

$$\pi_7 = sin(theta)\, S_u^a\, D_n^b\, v_f^c = (-)\,(mt^{-2}L^{-1})^a\,(L)^b\,(Lt^{-1})^c$$
$$= (m^a)\,(L^{-a}L^bL^c)\,(t^{-2a}t^{-c}) = m^a\,L^{-a+b+c}\,t^{-2a-c} \Rightarrow$$

$$\begin{aligned} \mathbf{m} &: 0 = a \rightarrow \mathbf{a = 0} \\ \mathbf{L} &: 0 = -a + b + c \rightarrow \mathbf{b = 0} \\ \mathbf{t} &: 0 = -2a - c \rightarrow \mathbf{c = 0} \end{aligned} \tag{7.11}$$

$$= sin(\theta)\, s_u^0\, D_n^0\, v_f^0 = sin(\theta)$$

The sixth step of the π theorem is to write the final functional relationship by using the solved dimensionless π groups above to transform Equation 7.12 into Equation 7.13:

$$\pi_1 = f(\pi_2, \pi_3, \pi_4, \pi_5, \pi_6, \pi_7) \tag{7.12}$$

Now substituting for π:

$$\frac{Z_c}{Dn} = f(\frac{P_d}{s_u}, \frac{s}{D_n}, \frac{u_j}{v_f}, \frac{\rho * v_f^2}{s_u}, \frac{g * D_n}{v_f^2}, sin(\theta)) \tag{7.13}$$

Identifying the forces contributing to the erosion: the dynamic pressure and the jetting velocity, which are expressed in the jet ratio and the ratio between the jetting velocity and the forward velocity ($\frac{P_d}{s_u}$ and $\frac{u_j}{v_f}$).

7

Considering the nozzle geometry and orientation the soil: ($sin(\theta)$, $\frac{s}{D_n}$) represents the effective diameter of the nozzle based on the jetting angle.

Given Equation 7.13, I can use linear regression to from an equation to estimate the erosion depth. Linear regression is a statistical method used to model the relationship between a dependent variable (or response) and one or more independent variables (or predictors). The goal of linear regression is to find the "best-fitting" linear relationship that minimizes the difference between the observed values of the dependent variable and the values predicted by the model. The result of linear regression is an equation of a straight line that represents the linear relationship between variables.

The general form of a simple linear regression equation is:

$$y = mx + b \tag{7.14}$$

where:

- y is the dependent variable,
- x is the independent variable,

- m is the slope of the line, and
- b is the y-intercept.

For multiple linear regression (involving more than one independent variable), the equation becomes:

$$y = a_0 + a_1 * x_1 + a_2 * x_2 + ... + a_n * x_n \tag{7.15}$$

where:

- $x_1, x_2, ..., x_n$ are the independent variable,
- a_0 is the y-intercept, and
- $a_1, a_2, ..., a_n$ are the coefficients representing the impact of each independent variable on the dependent variable.

My "y" term is my π_1 dimensionless group, my "x" terms are my other dimensionless pi groups, and I calculated my "a" coefficients using a "MATLAB" code I created using the data gathered from my experiments. The coefficients are listed in Table 7.2.

The substituted terms create the following equation:

$$Z_c = D_n * (a_0 + a_1 * \pi_2 + a_2 * \pi_3 + a_3 * \pi_4 + a_4 * \pi_5 + a_5 * \pi_6 + a_6 * \pi_7) \tag{7.16}$$

Table 7.2: List of the coefficients determined by linear regression of **??**.

Coefficient	**Value**
a_0	0.00014
a_1	0.46
a_2	0.088
a_3	0.0013
a_4	0
a_5	−0.048
a_6	−0.0066

I can see that a_0 is negligible and a_4 cancels out π_5. Consequently, I can substitute the rest of the coefficients and π groups to form Equation 7.17.

$$Z_c = D_n * (0.46 * \frac{P_d}{s_u} + 0.088 * \frac{s}{D_n} + 0.0013 * \frac{u_j}{v_f} - 0.048 * \frac{g * D_n}{v_f^2} - 0.0066 * sin(\theta)) \tag{7.17}$$

It is important to note that this is a simplified model, and the parameters could be influenced by additional factors not included in this equation. The parameters in Equation 7.17 should be determined based on experimental data and calibration to match real-world conditions. This derivation provides a starting point for modeling erosion depth based on the specified parameters.

The data calculated using Equation 7.17 can be seen in Section 7.1.3.

7.1.3. UPDATED FIGURES

The figures below are from Section 6.2 as well as updated figures using Equation 7.17. They are included here for ease of reference.

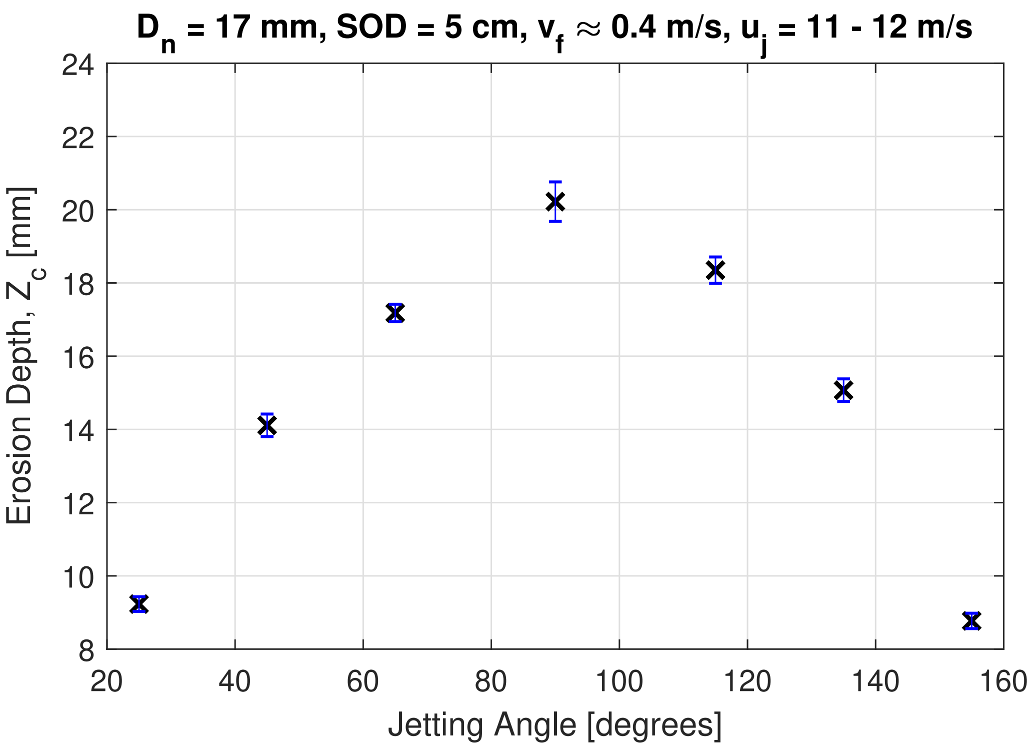

Figure 7.5: The average effects of jetting angle on the erosion depth, Z_c. The range markers for the data are indicated in blue and symbolize the standard deviations calculated during the experimental testing.

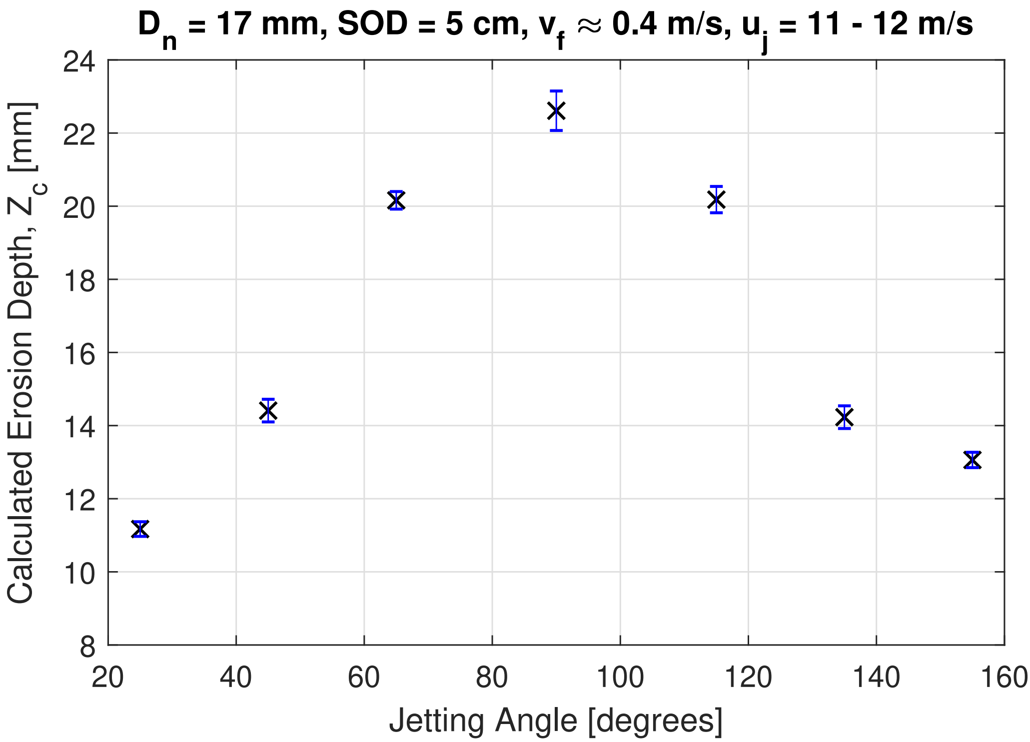

Figure 7.6: The effects of jetting angle on the erosion depth, Z_c using the Equation 7.17. The range markers for the data are indicated in blue and symbolize the standard deviations calculated during the experimental testing.

7

I was able to create Figure 7.6 using Equation 7.17. A similar bell curve is visible in both Figure 7.5 and Figure 7.6. As stated in Section 7.1.2, Equation 7.17 only provides an estimation for the erosion depth of cohesive soil. This is evident in Figure 7.6 since the erosion values do not appear exactly as the values in Figure 7.5.

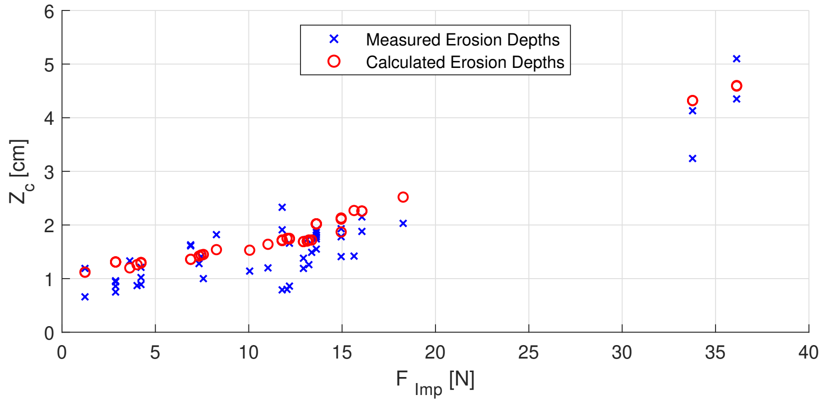

Figure 7.7: The relationship between the vertical Impingement Force, F_{Imp} $[N]$ and both the measured erosion depth from the experiments (blue) and the erosion depths calculated using Equation 7.17 (red).

Figure 7.7 is a modification of Figure 6.14 since it includes the erosion depths calculated using Equation 7.17. This figure displys how both the calculated and measured erosion depths follow the same trend. As vertical impingement force increases, so does the erosion depth. Figure 7.7 also lends support to Equation 7.17 as an accurate estimation for erosion depth.

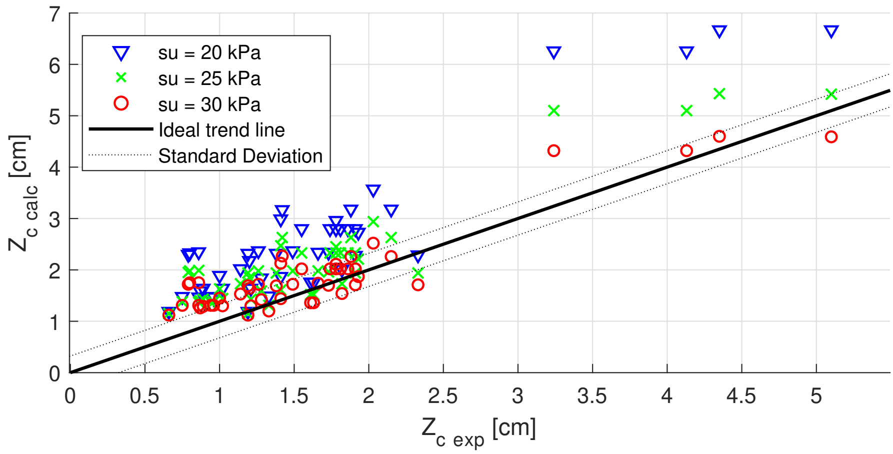

Figure 7.8: The calculated erosion depth, Zc_{calc} vs. the actual erosion depth, Zc_{exp}.

7

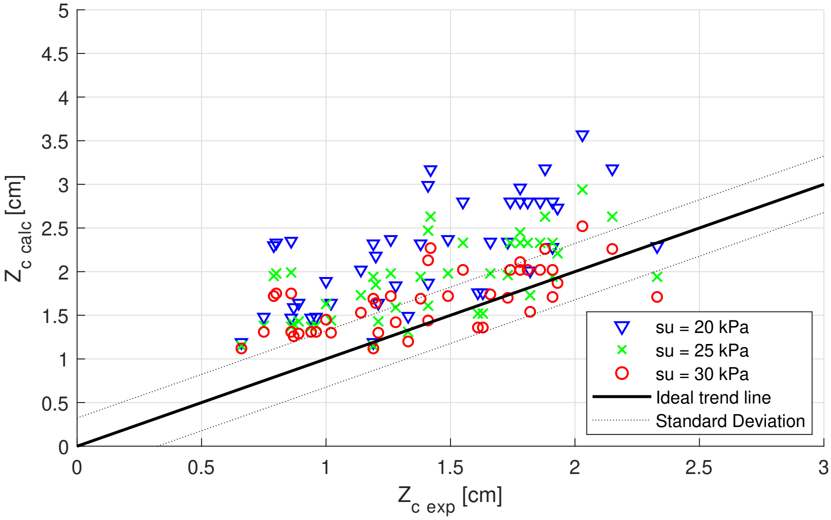

Figure 7.9: The calculated erosion depth, Zc_{calc} vs. the actual erosion depth, Zc_{exp} zoomed in on the majority collection of data.

Figure 7.8 and Figure 7.9 present a comparative analysis between the calculated erosion depths and the erosion depth measured during the experimental trials. This data-set allows an assessment of the precision and reliability of the calculated erosion depth values (using Equation 7.17 derived in Section 7.1.2). The "Standard Deviation" is based on the average standard deviation obtained during the experiments (Standard Deviation = 0.323). One can see that the calculated erosion depth overestimates the depth. Some overestimation is expected since natural conditions are difficult or impossible to re-create such as the exact composition of the clay, small variations in SOD, nozzle angle, or jetting velocity, the effects of water pressure, as well as any number of variables that come with dealing with real-world testing.

It is imperative to recognize that the cohesive soil employed in the experiments were characterized by an undrained shear strength spanning the range of 20 kPa to 30 kPa as documented in Figure 2.8. Notably, the calculated depths were predicated upon an assumed undrained shear strength value of 25 kPa. The data shown Figure 7.8 and Figure 7.9 suggests that the cohesive soil utilized in the experiments might have possessed a higher undrained shear strength than anticipated, potentially closer to 30 kPa. This observation underscores the importance of accurately characterizing the soil properties in experimental investigations, as variations in soil strength can significantly impact outcomes.

7.1.4. 1D-Approach

My third research objective was to contribute to the 1D-approach of Arnold Nobel's research by including the angle of the water jet as a parameter that will affect the jet cavity dimensions. Although the literal work of Nobel was not modified in a way that would allow me to characterize the work as nonetheless Nobel's 1D-approach, this thesis achieved a new way to estimate the jet cavity depth dimension while including the angle of the water jet as a parameter (Section 7.1.2), and a series of figures providing support to the reliability of this new method (Section 7.1.3).

A one-dimensional (1D) approach consists of using data such as line graphs, bar graphs or equations to derive an estimate. One can make erosion estimations based on the figures presented in this thesis. The figures in this study have reformed the way we look at the jetting angle of a water jet in the context of eroding cohesive soil.

Relevant industries may use the data provided in this thesis to better prepare and estimate erosion methods to fit the goals of future projects. For example, where a project requires minimal soil penetration or a more predictable sediment plume.

8

Conclusion and Recommendations

8.1. Conclusion

The conclusion derived from this thesis centers on the discernible impact of the water jet angle on the erosion process of cohesive soil. Probing the findings of this study, ranging from the erosion depth to the formation of the sediment plume, can be useful to inform various dredging processes. The versatility of this information becomes evident as it stands to contribute to the optimization of varied dredging methods, and offers tailored insights according to the specific objectives and requirements of the dredging process in question.

8.2. Recommendations

I offer the following recommendations for further study in the field of submerged inclined water jets. The first of these recommendations being the testing of full nozzles. Full nozzle testing would be a valuable next step to reinforce the work done in this thesis specifically, these nozzles should be tested in a pressure-controlled environment to better match the conditions of the sea-floor.

Additionally, further testing cohesive soils that have dissimilar undrained shear strengths may be enlightening. Testing different cohesive soils will expand the collected data and allow for more refined data in the field of inclined water jets. I would advise mixing the clay rather than using pre-formed clay when testing different soils. Mixing the clay will allow for more control of the undrained shear strength and other properties of the clay being tested.

Bibliography

[1] Albertson, M. L., Dai, Y., Jensen, R. A., & Rouse, H. (1950). Diffusion of submerged jets. Transactions of the American Society of Civil Engineers, 115(1), 639–664.

[2] Alhaddad, S., Mehta, D., & Helmons, R. (2023). Mining of deep-seabed nodules using a Coanda-effect-based collector. Results in Engineering, 17, 100852.

[3] Alhaddad, S., & Helmons, R. (2023). Sediment Erosion Generated by a Coanda-Effect-Based Polymetallic-Nodule Collector. Journal of Marine Science and Engineering, 11(2), 349.

[4] Backus, B. E. (2021, October). Triaxial shear testing of soils, understanding methods and equipment. GlobalGilson. Com.

[5] Bedón Vásquez, A. A. (2020). Quantifying the dispersion of turbidity currents generated by seafloor mining operations.

[6] Bharadwaj, R. S. (2019, July). Electromagnetic flow meters working principle - instrumentationtools. Inst Tools. Retrieved from https://instrumentationtools.com/electromagnetic-flow-meters-working-principle/

[7] Boschen-Rose, R. (2020). (pp. 1–151).

[8] Enthoven, D. H. B. (2021). Plume dispersion of low-density clayey suspension turbidity currents created by deep-sea mining.

[9] Farrar, D. M., & Coleman, J. D. (1967). The correlation of surface area with other properties of nineteen British clay soils. Journal of Soil Science, 18(1), 118–124.

[10] Fischer, H. B., List, J. E., Koh, C. R., Imberger, J., & Brooks, N. H. (1979). Mixing in inland and coastal waters. Academic press.

[11] Gauntner, J. W. (1970). Survey of literature on flow characteristics of a single turbulent jet impinging on a flat plate.

[12] Ghiabi, H., & Selvadurai, A. P. S. (2007). Laboratory testing of a soft silty clay. Soft Soil Engineering. Proc. of the 4th International Conference on Soft Soil Engineering, Vancouver, Canada. Taylor & Francis Group, London, 447–456.

[13] Halliday, D., Resnick, R., & Walker, J. (2013). Fundamentals of physics. John Wiley & Sons.

[14] IUCN issues brief, Deep-Sea Mining. (2022). IUCN Issues Briefs, (Deep-Sea Mining). Retrieved from https://www.iucn.org/sites/default/files/2022-07/iucn-issues-brief_dsm_update_final.pdf

[15] Kamal, E. (2017). Optimization of the fluidization system of the trailing suction hopper dredger.

[16] Kaolin, S. (2021, January). Kaolin Zettlitz Ia. Sedlecký kaolin a.s.

[17] Liu, X., Chen, X., Wei, J., Jin, S., Gao, X., Sun, G., ... Lu, Q. (2023). Study on sediment erosion generated by a deep-sea polymetallic-nodule collector based on double-row jet. Ocean Engineering, 285, 115220.

[18] Machin, J. B., & Allan, P. A. (2011). State-of-the-art jet trenching analysis in stiff clays. Frontiers in Offshore Geotechnics II, Proceedings of the 2nd International Symposium on Frontiers in Offshore Geotechnics, 871–876.

[19] Mitchell, J. K., Soga, K., & Others. (2005). Fundamentals of soil behavior (Vol. 3). John Wiley & Sons New York.

[20] Nobel, A. J. (2013). On the excavation process of a moving vertical jet in cohesive soil.

[21] Polymetallic Nodules (N.d.). - International Seabed Authority. Retrieved from https://www.isa.org.jm/files/documents/EN/Brochures/ENG7.pdf

[22] Rajaratnam, N. (1976). Turbulent jets. Elsevier.

[23] Reba, I. (1966). Applications of the Coanda effect. Scientific American, 214(6), 84–93.

[24] Rowe, P. W. (1962). The stress-dilatancy relation for static equilibrium of an assembly of particles in contact. Proceedings of the Royal Society of London. Series A. Mathematical and Physical Sciences, 269(1339), 500–527.

[25] Sharma, R. (2017). Deep-sea mining: Resource potential, technical and environmental considerations. Springer.

[26] Skempton, A. W. (1985). Residual strength of clays in landslides, folded strata and the laboratory. Geotechnique, 35(1), 3–18.

[27] Somerset Rivers Authority. (2020, July).

[28] Struck, D. (2018). Mining the Treasures of the Deep. World Ocean Forum. Retrieved from https://medium.com/world-ocean-forum/mining-the-treasures-of-the-deep-4dc06ed9d4df

[29] Terzaghi, K. (n.d.). 1943, Theoretical Soil Mechanics, John Wiley & Sons, New York.

[30] Townend, S. (2011, March). Soil Property Testing Limited. Eurocode 7. Retrieved from https://www.soilpropertytesting.com/EURO_CODE_7.html

[31] Van Rhee, C. (2010). Sediment entrainment at high flow velocity. Journal of Hydraulic Engineering, 136(9), 572–582.

[32] van Rhee, C. (2018, April). Lecture Notes OE44045. Prof. Dr. Ir. Cees van Rhee.

[33] Verhagen, H. J. (2000). Water injection dredging. 2nd International Conference Port Development and Coastal Environment: PDCE 2000, 5-7 June 2000, Varna, Bulgaria. Black Sea Coastal Association.

[34] Wang, B., van Rhee, C., Nobel, A., & Keetels, G. (2021). Modeling the hydraulic excavation of cohesive soil by a moving vertical jet. Ocean Engineering, 227, 108796.

[35] Weegenaar, R. A., Keetels, G. H., Winkelman, M. O., & van Rhee, C. (2015). Sand erosion with a traversing circular jet. Proceedings of the Institution of Civil Engineers-Maritime Engineering, 168, 76–83. Thomas Telford Ltd.

[36] White, F. M. (1990). Fluid mechanics. New York.

[37] Winterwerp, J. C., & Van Kesteren, W. G. M. (2004). Introduction to the physics of cohesive sediment dynamics in the marine environment. Elsevier.

[38] Wu, C. (2018). Erosion Mechanisms below a vertical plain Jet on a Non-Cohesive Soil Bed.

[39] Zhao, G., Xiao, L., Yue, Z., Liu, M., Peng, T., & Zhao, W. (2021). Performance characteristics of nodule pick-up device based on spiral flow principle for deep-sea hydraulic collection. Ocean Engineering, 226, 108818.